COHERENT MANIPULATION OF LIGHT IN THE CLASSICAL AND QUANTUM REGIMES VIA FOUR-WAVE MIXING BRAGG SCATTERING

A Dissertation

Presented to the Faculty of the Graduate School

of Cornell University

in Partial Fulfillment of the Requirements for the Degree of

Doctor of Philosophy

by

Alessandro Farsi

August 2015

COHERENT MANIPULATION OF LIGHT IN THE CLASSICAL AND QUANTUM REGIMES VIA FOUR-WAVE MIXING BRAGG SCATTERING

Alessandro Farsi, Ph.D.

Cornell University 2015

Nonlinear (NL) optics differs from its linear counterpart in that it drives interaction between different optical frequencies. In a stimulated parametric process, such as sum/difference frequency generation in $\chi^{(2)}$media or phase conjugation in $\chi^{(3)}$, a strong pump drives the interaction with a weaker signal field, and an idler field is generated at a different frequency set by the energy conservation of the process. In this work we focus on a subset of possible interactions, i.e. *frequency translations*, in which, for a generated idler, the signal undergoes depletion and the total energy of the two fields is conserved in the Manley-Row sense (i.e. number of photons is conserved). While for most applications such distinction is not fundamental, it becomes a crucial aspect in the very-low-power and quantum regimes.

The focus of this work is Bragg Scattering (BS) in $\chi^{(3)}$ medium, a parametric four wave mixing interaction where two pumps separated by an angular frequency detuning $\Delta\omega$ drive the interaction between a signal and an idler separated by the same amount. This configuration offers great flexibility with respect to choice of participating fields, enabling translation across both a wide span of wavelength and small detuning within the same frequency bands.

We first utilize BS to demonstrate an unusual phenomena known as *temporal cloaking*: a coherent optical manipulation that hides events from an observer. Using the concept of space-time duality, we implement a novel split time-lens that

opens and closes a gap in a continuous wave (CW) probing signal, in which events can happen undetected. The reversibility of frequency translation enables us to do and undo the gap without adding any noise.

Successively, we employ BS in the quantum regime: time-reversibility implies the preservation of quantum coherence so that quantum states can be manipulated without affecting their quantum nature. Frequency translation offers a way to connect elements operating at different wavelengths for a large scale quantum system. We use BS to operate on single photon states: we demonstrate high performance implementation using a nonlinear fiber, achieving efficient translation of 94 % while having low-losses and extremely low noise compared to previous demonstrations. With such system, we are able to implement more complex manipulation of the quantum field performing temporal compression and magnification using a time-lens.

Since frequency translation provides us with the ability to coherently couple arbitrary pairs of frequencies, it is natural to introduce the concept of *chromatic qubits*, a frequency encoding that is naturally controlled by BS. We manipulate such qubits using a sequence of two BS interactions in a Ramsey interferometer configuration: by varying the delay between the two stages, we observe fringes of interference between the two possible output frequency states.

Finally we propose an extension of BS to control high-dimensional frequency space, and study theoretically the different regimes of BS interaction in dense-multiplexed frequency channels in the presence of multiple pumps.

BIOGRAPHICAL SKETCH

Alessandro Farsi was born in the Italian city of Monza on November 24th, 1984. He grew up there, feeding his speculative mind with every science fiction book he can find in the local library. In 2003, at the age of 19, he enrolled at Universita' degli Studi di Milano - Bicocca, where he discovered that certain stories he read about quantum mechanics are not too far off from reality, and earned a Laurea Triennale (B. Physics equivalent) with a thesis on the *no-cloning thoerem* in quantum computation in 2006. Following his interests in quantum optics, he transfered to Universita' Statale di Milano, earning a Laurea Magistrale in Physics (M. Physics equivalent) in 2008. His thesis work on opto-mechanical microcavities was conducted at the LENS in Firenze.

He left for Ithaca, NY, USA on the 9th of August, 2009 where immediately joined Prof. Alexander Gaeta's Nonlinear and Quantum Optics group in the Cornell University School of Applied and Engineering Physics. At Cornell he explores four wave mixing phenomena to control classical signals and single photons, as part of his doctoral studies. He received a Master of Science degree from Cornell University in Spring 2013.

Soon her eye fell on a little glass box that was lying under the table: she opened it, and found in it a very small cake, on which the words 'EAT ME' were beautifully marked in currants. 'Well, I'll eat it,' said Alice, 'and if it makes me grow larger, I can reach the key; and if it makes me grow smaller, I can creep under the door; so either way I'll get into the garden, and I don't care which happens!'

Lewis Carrol *"Alice's Adventures in Wonderland"*

ACKNOWLEDGEMENTS

A first heartfelt thank you goes to Professor Alex Gaeta, who led me in this major endeavor, starting from my very first day in Cornell , through the years of success and failures, and the complication presented by my becoming a father, to the final achievement of this PhD. You created a wonderful, engaging and collaborative environment to pursue science, which I feel lucky to be part of. I treasure the passion, the advice and the many opportunities you gave me, as well as some "famous quotes" that I have already started to recycle.

This work would have not been possible without the extreme support of several colleagues with whom I had the great fortune to work with. Onur Kuzucu introduced me to the wonders of creating my own single photon detectors. Stephane Clemmen was a powerhouse of ingenuity and self-criticism. Moti Fridman shared a great amount of madness and bad Israeli music. Sven became my physics and coffee *sensei*. Yoshi Okawachi was the pillar of our scientific community: I still don't know how I managed to never be the butt of one of your pranks.

Our group is a den of smart minds, and I learned a lot from each of you: Mark, Pablo, Bongu, Vivek, Kasturi, Ryan, Micheal, Sam, Dan, Pratham, Mengjie, Adrea, Chaitali, Chaitanya, Henry, Gauri, Xiaohui. I'm grateful every discussion in front of a whiteboard, for every suggestion, for every shared meal, but also for the comical intramural basket, the photoshopped group pics, the high fives and the few ping pong matches. Sorry for all the Python evangelization and the Apple smash talk (but it was for a good reason)

Thanks to the Gaeta alumni network, and especially a shout to Imad and our missed quantum/Italian connection. Thanks to Prof. Michal Lipson and her entire research group - you really put a ring on it. In the last year, I've come to appreciated our 'quantum journal club (with cake)', which become a great moment

of sharing knowledge: we will make it happen in Manhattan.

I thank Prof. Frank Wise and Prof. Steve Marschner for agreeing to participate as my committee and helping me broaden the horizons of my knowledge.

Three cheers for my underwater hockey team: you were my oxygen! Vincent with his twin-cent, Laura after our chapter house discovery, Josh (sorry for all the injuries) and Enrico that introduced me to this silly sport.

Thanks to Jim and our odd friendship that slowly developed, Nick in all his forms ('awesome', 'enthusiastic' and 'creepy'), Yariv soul mate till the girls got between us. The physicists and their sleveless crazy parties and long boardgames. Elena and the undergrade scene.

The ITA people, first friends I had in this strange land: you all left, I finally leave too. Alkisti, I miss preparing you coffee and dinner. Thank to the Italian connection: you warmed me up with loud conversation on a night during my first Ithacan winter. Thank you for all the meal (free and not) shared together.

After 6 years, I managed to put some roots in Ithaca: thank to my new adopted family: Janice, John and Cheryl and the rest of the family. Thanks to you, Ithacans, Caitlin, Emily, Molly, Danny, Aaron, Winnie, Laura and more.. Your friendship relieved me from my home-sickness. May we have many more Grassroots together.

The further I go on this list, the farther I reach to those from whom I become distant. There is a toll to pay for living so far from your country and seeing the friends you make depart for even further destinations.

Grazie, amici lontani! I've missed you so much! Dr. Emanuele, Dr. Silvia, Dr. Michele, Dr. Paolo... much time has past since U2 (and even longer since I met some of you). Simone, Manfredda, Elia, Giulia, Federica and all the *zingari* of the aula Laser. Caterina, Lucia, Matteo, Luca, and Silvia II.

To my former advisors, Prof. Cattaneo and Prof. Marin who set my path a long time ago.

Alla Mamma e al Babbo (ormai Nonni) Penso di aver studiato abbastanza! To my brother Ado, on his parallel way to the highest degree. To all my larger family for whom I became "lo zio d'America'

And finally to Maya and Aviva, that changed my heart and my life as nothing else did before: just please call me Dr. Babbo!

In memory of the many APDs that gave their life for this work

CONTENTS

LIST OF FIGURES

CHAPTER 1

INTRODUCTION

1.1 Frequency Translation

Our everyday description of optical phenomena is linear: we represent light propagation as a ray that we can trace independently from any other ray, regardless of its intensity or color. Even the case of coherent light, where different paths can lead to interference patterns, can be described with linear equations. It is only when the intensity of the electromagnetic field is strong enough, compared with the electric field generated by the electronic cloud of a medium, that nonlinear effects arise.

Nonlinear (NL) optics differs from its linear counterpart in that it drives interaction between different optical frequencies [1]: NL phenomena can lead to the generation new colors, as in higher harmonic generation, where the new field is at a frequency multiple of the driving pump [2]; it can produce continuous spectral broadening of a field, to the limit of the generation of a 'supercontinuum' of frequencies [3]. In a stimulated parametric process, such as sum/difference frequency generation in $\chi^{(2)}$media or phase conjugation in $\chi^{(3)}$, a strong pump drives the interaction with a weaker signal field, and an idler field is generated at a different frequency set by the energy conservation of the process. This enables the generation of laser-like emission at wavelengths where gain medium is not available or the creation of sources of wide tunability such as Optical Parametric Oscillators and Amplifiers.

Moreover, modulations applied to the signal or to the pump are reflected in

the idler, and the process is often defined as *frequency conversion* [4]. Obviously many practical applications are found in high speed optical telecommunication, which relies heavily on wavelength multiplexing to achieve large data throughput, but also in other fields, such as far infrared and thermal imaging and spectroscopy [5, 6], in which hard to detect signals are converted to more convenient wavelengths.

Since the participating fields mix together, frequency conversion can be employed to perform all-optical operations on the signal. From simple logical operations that depend only on the intensity of the fields [7], to signal processing that takse advantage of the wave-like nature of light [8], frequency conversion enables all-optical manipulation of the optical signal, with two advantages over electronic-based solutions: much larger bandwidth and higher power efficiency.

In this work we focus on a subset of possible interactions, *frequency translations* or *frequency exchange* [9], in which, for a generated idler, the signal undergoes depletion and the total energy of the two fields is conserved, in the Manley-Row sense, (i.e. number of photons is conserved). While, for most applications, such distinction is not fundamental, it becomes a crucial aspect in the very-low-power and quantum regimes.

1.1.1 Organization of the work

Optical frequency translation can be achieved with different processes: notable examples are sum-frequency in nonlinear crystals [10], crossphase modulation in fibers, and via electro-optical and acusto-optical modulator. The focus of this work is Bragg Scattering (BS) in $\chi^{(3)}$ medium, a parametric four-wave mixing interaction (FWM) where two pumps at separate frequencies drive the interac-

tion between signal and idler. Originally it was observed in systems where two degenerate pumps, coming at different angles, formed through interference a periodic pattern that would scatter similarly to a Bragg grating. FWM interaction in a collinear configuration was not studied until the 1990s [11, 12], when it was noticed for its convenient properties of wide-band tunability and low noise transfer.

This dissertation is organized in the following

- In chapter 2, we formally derive BS interaction from the theory of nonlinear optics, and analyze different regimes of operation and phasematching conditions. We also introduce a quantized description of the process.
- In chapter 3, we show how BS enabled us to demonstrate temporal cloaking, a coherent optical manipulation that hides events from an observer. Using the concept of space-time duality, we implement a novel split-time-lens that opens or closes a gap in a CW probing signal. Because BS is reversible, with a second interaction we are able to canceling the effects of the first time-lens, making the cloaking undetectable.
- In chapter 4, we apply BS in the quantum regime: time-reversibility implies the preservation of quantum coherence so that quantum states can be manipulated without affecting their quantum nature. We use BS to operate on single photon states: first we demonstrate a low-noise implementation using a nonlinear fiber, then, using the same system, we implement time-lens manipulation over a single photon, performing temporal compression and expansion.
- In chapter 5, we introduce the concept of bichromatic qubits, i.e. a frequency encoding that is naturally controlled by BS. First, we manipulate such qubits using a sequence of 2 BS interactions in a Ramsey interferometer configura-

tion. Second, we propose an extension to high-dimensional space, and study theoretically the different regimes of BS interaction. We explore the case of many pumps coupling different frequency bins in nontrivial fashion.

- Finally, in chapter 6, we summarize the results and propose directions for future research.

CHAPTER 2

THEORY OF OPTICAL NONLINEAR INTERACTIONS AND BRAGG SCATTERING

The response of a material (or polarization P) in the presence of an external electric field E can be expressed as $P(t) = \epsilon_0 \bar{\chi}(E)\bar{E}(t)$ where χ is the polarizability of the medium. Indeed, $\bar{\chi}(E)$ can be expanded in Taylor's series, the first term being related to the relative dielectric constant $\epsilon_r = 1 + \chi^{(1)}$. Nonetheless, when the intensity of the electric field is strong enough, for example for collimated laser beam or concentrated inside a waveguide, the higher order terms become relevant leading to the nonlinear regime of light interaction. We can rewrite the equation separating a linear and a nonlinear contribution $P = P^{(1)} + P^{NL} = \epsilon_0 \bar{E} + \epsilon_0 \bar{\chi}^{(2)}_{i,j} E_i E_j + \epsilon \bar{\chi}^{(3)}_{i,j,k} E_i E_j E_k + \ldots$, [1] where $\bar{\chi}^{(i)}$ are, in general, tensors. For the vast majority of material (i.e. centrosymmetric), $\chi^{(2)}$ vanishes because of symmetries at the molecular level. On the other hand, $\chi^{(3)}$term, or Kerr nonlinearity, plays a dominant role in the dynamics of most materials, including the fibers considered in this work.

From Maxwell's equations of electromagnetism, one derives the wave equation for isotropic, dispersionless materials ([13] eq. (2.1.17))

$$\nabla^2 E(\bar{x}, t) - \frac{\epsilon_r}{c^2} \frac{\partial^2 E}{\partial t^2} = \frac{1}{\epsilon_0 c^2} \frac{\partial^2 P^{NL}}{\partial t^2}$$

In order to describe dispersive dynamics, regardless of whether the dispersion is introduced by the material or by the modal propagation (as in the case of

[1] $\chi^{(3)}$ is in general a tensor, but in the rest of the work, we will focus on isotropic materials and we will consider material response as a scalar.

a waveguide), one has to expand each field as the sum of its various frequency components

$$E(x,t) = \sum_n \sum_{\omega_n} E_n(\omega_n) e^{-i\omega_n t} e^{ik_n(\omega_n)x} + c.c.$$

$$E(x,t) = \sum_\omega E(\omega) e^{-i\omega t} + c.c.$$

So that we can rewrite a wave equation that holds for each ω

$$\nabla^2 E(\bar{x},\omega) - \frac{\epsilon_r(\omega)}{c^2}\frac{\partial^2 E(\bar{x},\omega)}{\partial t^2} = \frac{1}{\epsilon_0 c^2}\frac{\partial^2 P^{NL}(\bar{x},\omega)}{\partial t^2} \tag{2.1}$$

Let's now, for a moment, focus on the left hand of the equation and apply two important approximations.

First, we consider only a narrow part of the spectrum centered on a carrier angular frequency ω_0, so we can write $E(x,t) = A(x,t)e^{i\omega_0 t}$ where $A(x,t) = \int A(x,\omega)e^{i\omega t}$ is the pulse envelope and ω the baseband angular frequency.

Second, in the work presented here, light propagates and interacts in a waveguide (i.e. an optical fiber), which is an inhomogeneous medium that affects the spatial propagation. The waveguide defines specific spatial transverse modes while light propagates along the waveguide in the z-direction. The fields can now be expanded as the sum of the spatial modes: $A_\omega(x,\delta\omega) = \sum_n a_{k_n}(x,y)A_n(z,\delta\omega)e^{-i\omega t}e^{i\beta_n(\omega)z} + c.c.$. $a_{kn}(x,y)$ describe the transverse distribution of the mode and $\beta_n(\omega)$ the propagation constant for that mode. The analysis of the solution of waveguide modes can be found in [14, 15].

Plugging the two modal expansions into (2.1) we obtain the following

$$\frac{d^2A_n}{dz^2} + 2i\beta_n(\omega)\frac{dA_n}{dz} - \beta_n(\omega)^2 A_n + \\ - \frac{\epsilon_r(\omega_0)}{c^2}\left[\frac{\partial^2 A_n}{\partial t^2} + 2i\omega_0\frac{\partial A_n}{\partial t} - \omega_0^2 A_n\right] = \frac{\omega_0^2}{\epsilon_0 c^2}P^{NL}$$

We assume that A_n varies slowly with z and t so that the second derivative $\frac{d^2A_n(z,\omega)}{dz^2} \ll 2i\beta_n(\omega)\frac{dA_n(z,\omega)}{dz}$ as well $\frac{\partial^2 A_n}{\partial t^2} + 2i\omega_0\frac{\partial A_n}{\partial t} \ll \omega_0^2 A_n$as can be ignored (*slowly varying envelope*). Such approximation holds for P_{NL} as well.

$$2i\beta_n(\omega)\frac{dA_n}{dz} + \left[\beta_n(\omega)^2 - \frac{\omega_0^2\epsilon_r(\omega_0)}{c^2}\right]A_n = \frac{\omega_0^2}{\epsilon_0 c^2}P^{NL}$$

It is now useful to expand in Taylor series the propagation constant $\beta_n(\omega) = \sum \frac{1}{n!}\beta^{(i)}|_{\omega_0}(\omega - \omega_0)^n$, and identify the first few terms: $\beta^{(0)} = 1/c$ relates directly to the index of refraction, $\beta^{(1)} = 1/v_g$ is the inverse of the group velocity and $\beta^{(2)}$ is called group velocity dispersion (GVD).

We also notice that

$$\sqrt{\frac{\omega_0^2\epsilon_0\epsilon_r(\omega_0)}{c^2}} = \beta(\omega_0) = \beta^{(0)}$$

and

$$\beta(\omega)^2 - \left(\beta^{(0)}\right)^2 \approx 2\beta^{(0)}\left[\beta(\omega) - \beta^{(0)}\right].$$

so that

$$2i\beta(\omega)\frac{dA_n}{dz} + 2\beta^{(0)}\left[\beta(\omega) - \beta^{(0)}\right]A_n = \frac{\omega_0^2}{\epsilon_0 c^2}P^{NL}$$

and expanding for $\beta(\omega)$

$$\frac{dA_n}{dz} + i\beta^{(1)}(\omega - \omega_0)A_n + i\frac{\beta^{(2)}}{2}(\omega - \omega_0)^2 A + \ldots = \frac{\omega_0^2}{\epsilon_0 c^2} P^{NL}$$

Those terms in ω can be turned via formal integration into derivatives with respect to time $(\omega - \omega_0) \to i\frac{\partial}{\partial t}$.

$$\frac{dA_n}{dz} - \beta^{(1)}\frac{\partial A_n}{\partial t} + i\frac{\beta^{(2)}}{2}\frac{\partial^2 A_n}{\partial t^2} + \ldots = \frac{\omega_0^2}{\epsilon_0 c^2} P^{NL}$$

Higher order of $\beta(\omega)$ expansion would lead to higher order derivatives, but in this work, we can truncate at $\beta^{(2)}$ without losing accuracy.

To simplify the equation we introduce a coordinate transformation $\tau = t - z/v_g = t - \beta^{(1)}z$ so that for the new reference frame $A_n = A_n(z, \tau)$

$$\frac{dA_n}{dz} + i\frac{1}{2}\beta^{(2)}\frac{\partial^2 A_n}{\partial \tau^2} = i\frac{\omega}{nc} P^{NL}$$

From now on, we consider only $\chi^{(3)}$ process so that $P^{NL}(x,t) = \chi^{(3)} |E(x,t)|^2 E(x,t)$. When expanded into the spatial and frequency modes introduced earlier, we obtain the following *nonlinear Schrodinger equation*

$$i\frac{d}{dz}A = \frac{1}{2}\beta^{(2)}\frac{\partial^2}{\partial \tau^2}A - \gamma |A|^2 A \tag{2.2}$$

where $\gamma = \frac{\chi^{(3)} 4\pi}{\omega_0 a}$ is the nonlinear interaction parameter: a depends on the spatial mode overlap. For telecommunication optical fibers, $\gamma = 0.5 - 10 W^{-1} km^{-1}$.

Let's now see how different frequencies can interact in a nonlinear medium: we

can expand field A as the sum of four different fields

$$A(z,\tau) = A_1(z,\tau)e^{-i\Delta\omega_1\tau+i\beta(\omega_1)z} + A_2(z,\tau)e^{-i\Delta\omega_2\tau+i\beta(\omega_2)z} + \\ + A_3(z,\tau)e^{-i\Delta\omega_3\tau+i\beta(\omega_3)z} + A_4(z,\tau)e^{-i\Delta\omega_4\tau+i\beta(\omega_4)z}. \quad (2.3)$$

where $\Delta\omega_i = \omega_i - \omega_0$ denotes the difference in frequency between each field and the carrier.

We can plug equation (2.3) into (2.2), obtaining an equation that varies in time. We can separate the equation into a system of four equations, one for each interacting field and time varying exponential: the nonlinear term is selected when

$$i\frac{d}{dz}A_i \quad = -\beta^{(2)}(\omega_i)\frac{\partial^2}{\partial\tau^2}A_i \quad +\gamma \sum_{\pm\omega_j\mp\omega_k\pm\omega_i=\omega_i} e^{i\kappa_{i,j,k,l}z}A_jA_k^*A_l \\ i = 1,2,3,4 \qquad A_i \equiv A(z,\tau) \qquad (2.4)$$

In this expansion we make the assumption that, for each of the fields, bandwidth is small enough that we can only consider chromatic dispersion at each field center frequency, i.e. $\beta^{(2)}(\omega_i) \gg \beta^{(3)}(\omega_i)\delta\omega_i$.

On the other hand, the energy separation of different fields may be substantially large so that a higher order needs to be taken into account when calculating the phase mismatch $\kappa_{i,j,k,l} = \sum \pm\beta(\omega_i)$, i.e $\beta(\omega) = \sum_i \frac{\beta^{(i)}}{i!}(\omega-\omega_0)^i$

The nonlinear term in general produces a mixing of the different frequencies. The condition on the sum $\pm\omega_j\mp\omega_k\pm\omega_i = \omega_i$ is related to the energy conservation of the Four Wave Mixing (FWM) process: three fields frequencies add up to produce a fourth field. Whereas for any set of interacting fields, many different interactions are possible, in general most of them are negated by the phase-matching term $e^{i\kappa_{i,j,k,l}z}$.

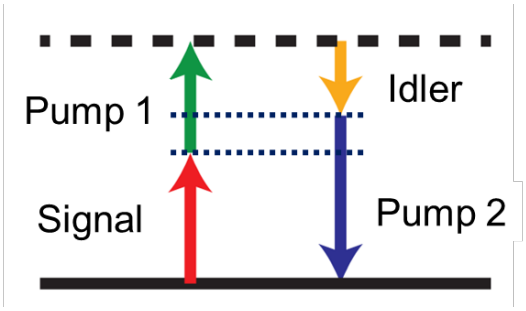

Figure 2.1: Energy levels depiction of FMW Bragg Scattering

Equation (2.4) provides a good approximation for most of $\chi^{(3)}$ process: for example $\omega_1 = -\omega_2 = \omega_3$ and $\omega_4 = 3\omega_1$ describes Third Harmonic Generation. Some processes, like self-phase modulation $\omega_1 = \omega_2 = \omega_3 = \omega_4$, and cross-phase modulation (XPM) $\omega_1 = \omega_2, \omega_3 = \omega_4$ are always phasematched.

2.1 Bragg Scattering

Let's now concentrate on a specific parametric process, known as Bragg Scattering (BS) [12]: we identify two strong pump fields $A_{p1}$and A_{p2}at $\omega_{p_1}$and ω_{p2}, and two weak fields $A_s$and A_i respectively signal and idler, with the idler frequency such that $\omega_s - \omega_i = \omega_{p1} - \omega_{p2} = \Delta\Omega$ is the amount of frequency translation. The general evolution of the four fields is

$$
\begin{aligned}
i\frac{d}{dz}A_{p1} &= \frac{\beta^{(2)}(\omega_{p1})}{2}\frac{\partial^2}{\partial\tau^2}A_{p1} - \gamma\sum_{p1,p2,s,i} e^{+i\kappa_{p1,p2,s,i}z} A A_k^* A_l \\
i\frac{d}{dz}A_{p2} &= \frac{\beta^{(2)}(\omega_{p2})}{2}\frac{\partial^2}{\partial\tau^2}A_{p2} - \gamma\sum_{p1,p2,s,i} e^{+i\kappa_{p1,p2,s,i}z} A A_k^* A_l \\
i\frac{d}{dz}A_{s} &= \frac{\beta^{(2)}(\omega_{s})}{2}\frac{\partial^2}{\partial\tau^2}A_{s} \quad - \gamma\sum_{p1,p2,s,i} e^{+i\kappa_{p1,p2,s,i}z} A A_k^* A_l \\
i\frac{d}{dz}A_{i} &= \frac{\beta^{(2)}(\omega_{i})}{2}\frac{\partial^2}{\partial\tau^2}A_{i} \quad - \gamma\sum_{p1,p2,s,i} e^{+i\kappa_{p1,p2,s,i}z} A A_k^* A_l
\end{aligned}
$$

We operate now three approximations: first, most of the nonlinearity inter-

action is driven by the pump fields, i.e. $|P|^2 \gg |A_{s,i}|^2$, second, pump fields are not depleted by the interaction nor modified by dispersion; third, dispersion is small enough that it does not affect the temporal shape of the interacting fields (quasi-CW approximation).

The system becomes now

$$\begin{aligned}
A_{p1}(z) &= e^{i\gamma\left(|A_{p1}|^2+2|A_{p2}|^2\right)z} A_{p1}(0) \equiv e^{i\Gamma_1 z} A_{p1} \\
A_{p2}(z) &= e^{i\gamma\left(2|A_{p1}|^2+|A_{p2}|^2\right)z} A_{p2}(0) \equiv e^{i\Gamma_2 z} A_{p2} \\
\frac{d}{dz}A_s(z) &= i2\gamma\left[\left(|A_{p1}|^2+|A_{p2}|^2\right)A_s(z) + \left(e^{+i\kappa z}A_{p1}(z)A_{p2}^*(z)\right)A_i(z)\right] \\
\frac{d}{dz}A_i(z) &= i2\gamma\left[\left(|A_{p1}|^2+|A_{p2}|^2\right)A_i(z) + \left(e^{-i\kappa z}A_{p1}^*(z)A_{p2}(z)\right)A_s(z)\right]
\end{aligned}$$

where $\kappa = \beta(\omega_s) - \beta(\omega_i) - \beta(\omega_1) + \beta(\omega_2)$ is the BS phase-matching term.

We can solve the system exactly: first we introduce the fields

$$A_{s,i}(z) = exp\left[i\gamma(|A_{p1}|^2+|A_{p2}|^2)z\right] B_{s,i}(z)$$

to include effects of cross-phase modulation. This nonlinear phase, being identical for the two fields, can be ignored in the following.

$$\begin{aligned}
\frac{d}{dz}B_s(z) &= i2\gamma\left[e^{-i(\kappa+\Gamma_1-\Gamma_2)z}A_{p2}A_{p2}^*\right]B_i(z) \\
\frac{d}{dz}B_i(z) &= i2\gamma\left[e^{-i(\kappa+\Gamma_1-\Gamma_2)z}A_{p2}^*A_{p2}\right]B_s(z)
\end{aligned}$$

In the case of pumps with equal power, i.e. $A_{p1} = \sqrt{P}e^{i\phi_{p1}}$, $A_{p2} = \sqrt{P}e^{i\phi_{p2}}$, the system takes a simpler form

$$\begin{aligned}
\frac{d}{dz}B_s(z) &= i2\gamma P e^{+i\kappa z}e^{i(\phi_{p1}-\phi_{p2})}B_i(z) \\
\frac{d}{dz}B_i(z) &= i2\gamma P e^{-i\kappa z}e^{-i(\phi_{p1}-\phi_{p2})}B_s(z)
\end{aligned}$$

Let's notice here that the phase of the pump is transferred to the converted fields as expected by FWM. The implication of this fact will be explored in the time-lens (chapter 3) and in the Ramsey interferometer (chapter 4), but they will be considered fixed in the following discussion, and incorporated in the definition of $B_{s,i}$

The trial solution of the system is $B_{s,i}(z) = C_1 \cos(k_{bs} z) + C_2 \sin(k_{bs} z)$, and together with the initial condition leads to the following system describing the evolution of the fields:

$$\begin{aligned} B_s(z) &= \left[\cos(k_{bs}z) + i\frac{\kappa}{k_{bs}}\sin(k_{bs}z)\right] B_s(0) + \left[i\frac{r}{k_{bs}}\sin(k_{bs}z)\right] B_i(0) \\ B_i(z) &= \left[-i\frac{r}{k_{bs}}\sin(k_{bs}z)\right] B_s(0) + \left[\cos(k_{bs}z) - i\frac{\kappa}{k_{bs}}\sin(k_{bs}z)\right] B_i(0) \end{aligned} \tag{2.5}$$

where $r = 2\gamma P$ is the coupling strength term and $k_{bs} = \sqrt{\kappa^2 + r^2}$ the scattering wavevector. We can define the conversion efficiency for an interaction length L as $\eta = \frac{r^2}{k_{bs}^2}\sin(k_{bs}L)^2$

In figure (2.2) we plot the evolution of the fields for different values of ratio between phase-matching and gain, versus propagation distance L. Let's notice here that, in the case of perfect phasematching, efficiency reduces to $\eta = \sin(rL)^2$, so that for $rL = \pi/2$ it leads to $\eta = 100$ %, full conversion between signal and idler, while for $rL = \pi/4$ the fields are mixing together ($\eta = 50$ %).

We now shift the focus to the phasematching term: it is convenient to expand at the zero dispersion frequency ω_{ZDW} (i.e. $\beta^{(2)}(\omega_{ZDW}) = 0$) so that $\beta(\omega) = \frac{\beta^{(3)}}{6}(\omega - \omega_{ZDW})^3 + \frac{\beta^{(4)}}{24}(\omega - \omega_{ZDW})^4 + o((\omega - \omega_{ZDW})^5)$, and to introduce the average pump frequency $\Delta\Omega = (\omega_{p1} + \omega_{p2})/2 - \omega_{ZDW}$, the frequency shift $\Delta\omega = (\omega_{p2} - \omega_{p1})$ and the signal offset ϵ_ω so that $\omega_s = \epsilon_\omega + \frac{\Delta\omega}{2} - \Delta\Omega$ and $\omega_i = \epsilon_\omega - \frac{\Delta\omega}{2} - \Delta\Omega$ (see

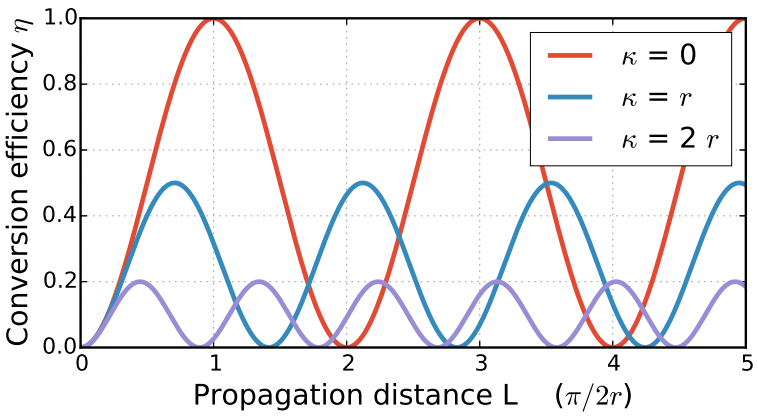

Figure 2.2: Evolution of two fields coupled by Bragg Scattering for different values the phasematching term $\kappa = 0,\ r,\ 2r$

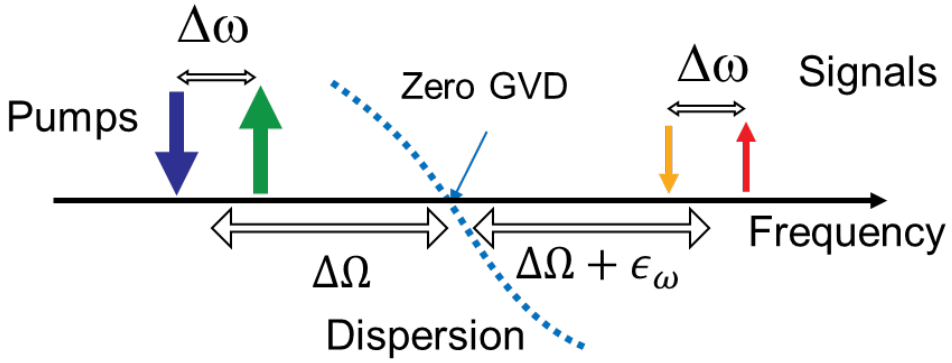

Figure 2.3: Cartoon of wavelength participating the interaction with respect to the zero dispersion wavelength.

figure 2.3). The phasematching now reads

$$\kappa = \frac{\beta^{(3)}}{6}\Big[\left(\epsilon_\omega - \frac{\Delta\omega}{2} - \Delta\Omega\right)^3 - \left(\epsilon_\omega + \frac{\Delta\omega}{2} - \Delta\Omega\right)^3 + \\ - \left(-\frac{\Delta\omega}{2} + \Delta\Omega\right)^3 + \left(+\frac{\Delta\omega}{2} + \Delta\Omega\right)^3\Big] + \\ \frac{\beta^{(4)}}{24}\Big[\left(\epsilon_\omega - \frac{\Delta\omega}{2} - \Delta\Omega\right)^4 - \left(\epsilon_\omega + \frac{\Delta\omega}{2} - \Delta\Omega\right)^4 + \dots \\ - \left(-\frac{\Delta\omega}{2} + \Delta\Omega\right)^4 + \left(+\frac{\Delta\omega}{2} + \Delta\Omega\right)^4\Big]$$

$$\kappa = \frac{\beta^{(3)}}{6}\left[3\Delta\omega\left(\epsilon_\omega - 2\Delta\Omega\right)\epsilon_\omega\right] + \\ \frac{\beta^{(4)}}{24}\left[\Delta\omega\left(\epsilon_\omega - 2\Delta\Omega\right)\left(\Delta\omega^2 + 4\Delta\Omega^2 - 4\Delta\Omega\epsilon_\omega + 4\epsilon_\omega^2\right)\right] + \dots$$

The most straightforward solution is when $\epsilon_\omega = 0$: $\beta^{(3)}$ term (as well as all the other odd terms) cancels out, leaving the smaller contribution from higher order dispersion.

For small ϵ_ω , approximating $\Delta\Omega_p \gg \Delta\omega \gg \epsilon_\omega$ we obtain

$$\kappa(\epsilon_\omega)\cdot L = \beta^{(3)}\Delta\Omega\Delta\omega\epsilon_\omega + \frac{\beta^{(4)}}{24}\left[8\Delta\omega\Delta\Omega^3\right] = \left(\epsilon_\omega + \Delta\epsilon\right)/\delta\omega_{bs}$$

And we define $\delta\omega_{bs} = L\cdot\beta^{(3)}\Delta\Omega\Delta\omega$ the acceptance bandwidth and $\Delta\epsilon = \frac{\beta^{(4)}}{3\beta^{(3)}}\Delta\Omega^2$ the frequency shift of the optimal conversion due to higher order dispersion. As a reference, $\beta^{(3)}\Delta\Omega \propto \beta^{(2)}|_{\omega_0+\Delta\Omega}$, so that the previous parameters can be expressed as function of dispersion at the fields wavelength, rather than at ω_{ZDW}.

To summarize: whereas different values of $\beta^{(3)}$ do not impact the optimal phasematching frequency, large absolute values reduce the acceptance bandwidth. Large

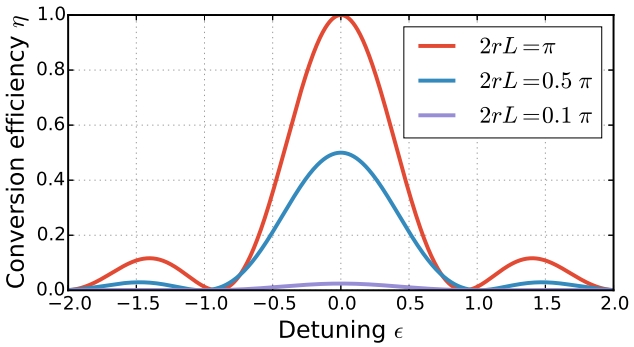

Figure 2.4: Bragg Scattering conversion efficiency versus detuning from the optimal phasematching for different pump power.

$\beta^{(4)}$ dispersion leads to an asymmetry of the optimal frequency across the ω_{ZDW}. It was also suggested [16] that large $\beta^{(4)}$ leads to a different solution where the fields sit across the $\beta^{(3)} = 0$ dispersion point (i.e. the apex of the dispersion curve) [?, 17].

Observing $\kappa(\epsilon_\omega)$ we understand that BS is a *selective* process. That is, for any pairs of target signal and idler frequencies it is always possible to find a phase-matched configuration, by virtue of the fact that with two pumps it is possible to independently tune $\Delta\Omega$ and $\Delta\omega$.

In figure 2.4 we plot the phasematching curves (i.e. the efficiency $\eta(\epsilon_\omega)$ as function of frequency offset ϵ_ω) , for the normalized parameters $\bar{\epsilon} = \epsilon_\omega/\Delta\omega$, $\bar{\delta\omega} = \delta\omega_{bs}/\Delta\omega = 1/\beta^{(3)}\Delta\Omega$ and $\bar{\Delta\epsilon} = \Delta\epsilon/\Delta\omega = \frac{\beta^{(4)}\Delta\Omega_p^3}{3}\delta\omega_{bs}$, and the constant parameter $\Delta\Omega = 100\Delta\omega$‘ fixed dispersion and different nonlinear gain;

The case when $\delta\omega_{bs} > \Delta\omega$, (i.e. $\bar{\delta\omega} > 1$) needs a different analysis, because it implies that idler field can be coupled by the same process to a different wavelength. This cascaded process can generate a “comb” of frequencies [18], and needs to be treated with a system of coupled equations, one for each line. This process limits the ability to achieve perfect transfer of the energy of the signal to a single idler,

hence it is usually considered a detrimental effect. We will explore more of the cascaded dynamics in section 5.2.

2.2 Quantum treatment

A quantum-mechanical theory of light is based on the operators of creation and annihilation of photon $\hat{a}_j^\dagger$ and $\hat{a}_j$ for the mode j that are the direct result of the quantization of the electromagnetic field A_j and A_j^* [19].

These operators are defined such that $\hat{a}_j^\dagger|n\rangle_j = \sqrt{n+1}|n+1\rangle_j$ and $\hat{a}_j|n\rangle_j = \sqrt{n}|n-1\rangle_j$, and obey to the boson commutation rules $[\hat{a}_i, \hat{a}_j] = 0$ and $\left[\hat{a}_i, \hat{a}_j^\dagger\right] = \delta_{i,j}$.

With the proper definition of units so that the number operator $\hat{N}_j = \hat{a}_j^\dagger \hat{a}_j$ measures the intensity in units of number of photons, the system derived in 2.5 correctly describes the evolution of the quantum operators associated with the signal and idler field (respectively $\hat{a}_s$ and $\hat{a}_d$) in the Heisenberg picture

$$\begin{bmatrix} \hat{a}_s(L) \\ \hat{a}_i(L) \end{bmatrix} = \mathfrak{Bs}(L) \begin{bmatrix} \hat{a}_s(0) \\ \hat{a}_i(0) \end{bmatrix} = \\ = \begin{bmatrix} \cos(k_{bs}L) + i\frac{\kappa}{k_{bs}}\sin(k_{bs}L) & i\frac{e}{k_{bs}}\sin(k_{bs}L) \\ -i\frac{e}{k_{bs}}\sin(k_{bs}L) & \cos(k_{bs}L) - i\frac{\kappa}{k_{bs}}\sin(k_{bs}L) \end{bmatrix} \begin{bmatrix} \hat{a}_s(0) \\ \hat{a}_i(0) \end{bmatrix} \quad (2.6)$$

.

The evolution is a unitary matrix, in fact we can write $\mathfrak{Bs}(L) = \begin{bmatrix} \mu & \nu \\ -\nu^* & \mu^* \end{bmatrix}$ and observe that $|\mu|^2 + |\nu|^2 = 1$, $\mathfrak{Bs}(L)^{-1} = \mathfrak{Bs}(L)^\dagger$ and $\mathfrak{Bs}(L)\mathfrak{Bs}(L)^{-1} =$ for

any value of γ,κ and L.

One can prove that it preserve the total number of photons, that is, no intensity noise is generated by the process. In fact, if we define the total photon number operator $\hat{N}(z) = \left\langle \overline{\hat{a}^\dagger}(L) \cdot \overline{\hat{a}}(L) \right\rangle = \sum_i \hat{a}_i^\dagger(L)\hat{a}_i(L)$ as a scalar product of the field operators, from simple algebra one obtains $\hat{N}(L) = \left\langle \overline{\hat{a}^\dagger}(L) \cdot \overline{\hat{a}}(L) \right\rangle = \mathfrak{B}_\mathfrak{s}(L)^{-1}\mathfrak{B}_\mathfrak{s}(L) \left\langle \overline{\hat{a}^\dagger}(0) \cdot \overline{\hat{a}}(0) \right\rangle = \left\langle \overline{\hat{a}^\dagger}(0) \cdot \overline{\hat{a}}(0) \right\rangle = \hat{N}(0)$. With similar argument, one can verify it preserves all the momentum.

For perfect phasematching (i.e. $\kappa = 0$), (2.6) describes a generic rotation between the two frequency modes. For $e = \pi/2$ it is equivalent to a beam-splitter acting on spatial modes and as a such it can be used to mix fields at different wavelengths.

In its more general form, equation (2.6) resembles the coupling between two energy levels of an atom caused by an external field close to resonance: the nonlinear strength and the phasematching take the role of the field strength and the frequency detuning [20]. This analogy will be further expanded in section 5.1 when describing the Ramsey interferometer.

A generic approach for broadband fields is given in [21]: we identify the input and output creation operators for each frequency ω, $\hat{a}_\omega^\dagger(0)$ and $\hat{a}_\omega^\dagger(L)$ and then find the Green function $G(\omega, \omega')$ for which

$$\hat{a}_\omega^\dagger(0) = \int d\omega' G(\omega, \omega')\hat{a}_\omega^\dagger(L).$$

By performing a Schmidt (singular-value) decomposition on the G function [22], we can extract a set of operators (separating the frequency range around

signal and idler) $\{a_s^{(k)}(\omega), a_i^{(k)}(\omega)\}_k$ coefficients ρ_k, τ_k for which each pair of mode operators undergoes a beam-splitter-like transformation

$$\begin{bmatrix} \hat{a}_s^{(k)}(L) \\ \hat{a}_i^{(k)}(L) \end{bmatrix} == \begin{bmatrix} \tau & \rho \\ -\rho^* & \tau^* \end{bmatrix} \begin{bmatrix} \hat{a}_s^{(k)}(0) \\ \hat{a}_i^{(k)}(0) \end{bmatrix}.$$

CHAPTER 3

TEMPORAL CLOAKING.

Recent research has uncovered a remarkable ability to manipulate and control electromagnetic fields to produce effects such as perfect imaging and spatial cloaking [23, 24]. To achieve spatial cloaking, the index of refraction is manipulated to flow light from a probe around an object in such a way that a 'hole' in space is created, and the object is hidden [25, 26, 27, 28, 29, 30, 31, 32, 33, 34, 35, 36].

Alternatively, it may be desirable to cloak the occurrence of an event over a finite time period, which leads to the idea of *temporal cloaking*[1], in which the dispersion of the material is manipulated in time, producing a 'time hole' in the probe beam to hide the occurrence of the event from the observer. This approach is based on accelerating the front part of a probe light beam and slowing down its rear part to create a well controlled temporal gap inside which an event occurs. The probe beam is then restored to its original form by the reverse manipulation of the dispersion such that the probe beam is not modified in any way by the event.

3.1 Theory of temporal cloaking

Detection of an object or an event is often performed by measuring a change in the properties of a light probe that interacts with the object or with elements participating in the event. The idea of spatial cloaking consists of the probe light being bent in a precise fashion to prevent it from being scattered by the object, which thus remains hidden from an observer. This has been done typically through use of exotic materials, such as ones with a negative index of refraction, or through

[1]This chapter is adapted from [37]

sophisticated manipulation of the refractive index [29, 30, 24]. Analogously, it is possible to cloak an event in the time domain from an observer by manipulating the dispersion of a material such that a temporal gap is created in the probe beam: any event that occurs within this gap does not modify the temporal/spectral properties of the probe beam and thus remains undetected [38]. This requires rapid changes in the dispersion and a recently proposed approach [38] involves the use of optical fibers that are pumped to high-power levels to produce large changes in the intensity-dependent refractive index. However, at such powers, other optical processes such as stimulated Raman and Brillouin scattering, could limit the ability to achieve cloaking. We propose an alternative means of creating the conditions that allow for temporal cloaking in which we apply concepts from the space–time duality associated with diffraction and dispersion [39].

To produce the time gap necessary to achieve temporal cloaking, we create a temporal element that imparts a suitable nonlinear frequency chirp on a probe beam over a time window in which the gap will be produced. After propagating through a dispersive element, the different frequency components of the probe created by the nonlinear chirp are advanced and retarded as required to produce the desired temporal gap. We create such a temporal element by implementing a split time-lens (STL) which is composed of two half time-lenses connected at the tips. This temporal element is created by FWM-BS with two pump in which the wavelength of one pump is constant in time and the other pump is pulsed and has a linear frequency chirp. To produce the appropriate chirp on the pump wave that will lead to a temporal gap, the red and blue spectral components of the pump pulse are separated and delayed with respect to each other. It is this step that splits the time lens to create the STL.

3.2 Time-lens

Space–time duality represents the analogy between spatial diffraction and temporal dispersion that arises from the mathematical equivalence between the equations describing the diffraction of a monochromatic beam in an isotropic medium

$$i\frac{d}{dz}A = -\frac{1}{2k}\frac{\partial^2}{\partial x^2}A$$

where k is the propagation constant, and the one-dimensional temporal propagation of a pulse through a dispersive medium [40, 39] (see equation (2.2) in absence of nonlinearity)

$$i\frac{d}{dz}A = \frac{1}{2}\beta^{(2)}\frac{\partial^2}{\partial \tau^2}A.$$

We immediately see that both the diffraction and dispersion operators impart a phase that is quadratic with respect to spatial and baseband angular frequency. We can write the effect of propagation over a distance L (for a total dispersion $\Phi = \frac{\beta^{(2)}L}{2}$) using the dispersion operator

$$U_\Phi[A] = F^{-1}[A(\delta\omega)e^{-i\Phi\delta\omega^2}] = \int exp(-i\delta\omega(t'-t))e^{-i\Phi\delta\omega^2}A(t')dt'd\omega$$

.

For large Φ, we obtain the Fraunhofer regime of chirped pulses

$$U[A] = exp\left(-i\frac{\tau^2}{2\Phi}\right)\int exp(-i\frac{\tau}{\Phi}t')A(t)dt$$

.

Similar to a regular thin lens that imparts a quadratic phase in space, a time-lens imparts a quadratic phase shift in time [41, 42, 43]. Time-lenses can be created with an electro-optic modulator or via a parametric nonlinear optical process such as four-wave mixing with a chirped pump. For BS, the idler field generated depends to the mix of all 3 fields $A_i(\tau) \propto A_s(\tau)P_1^*(\tau)P_2(\tau)$ (we are neglecting effect introduced by aperture $P(\delta\omega) \geq A(\delta\omega)$ and phasematching). The advantage of using nonlinear optics over electronic modulation is the very large chirping that can be to the signal field.

An imaging system is always composed of two distances p before and q after the lens, in which the image is allowed to diffract: in the time analogue, short pulses are dispersed by Φ_p before and Φ_q after the interaction with the time-lens.

We can write an expression for the idler at the imaging plane:

$$
\begin{aligned}
A_i(\tau) &\propto U_{\Phi p}\left[U_{\phi q}[A_s]U_{\phi 1}[P_1]U_{\Phi 2}[P_2]\right] \\
&= F^{-1}\left\{\left[A(\delta\omega)exp(-i\Phi\delta\omega^2) * \left[exp(i\Phi_1\delta\omega^2) * exp(-i\Phi_2\delta\omega^2)\right]\right] exp(-i\Phi\delta\omega^2)\right\}
\end{aligned}
$$

$$
\begin{aligned}
&\propto F^{-1}\left\{\left[A(\delta\omega)exp(-i\Phi\delta\omega^2) * exp\left(-i\frac{\Phi_{p1}\Phi_{p2}}{\Phi_{p1}-\Phi_{p2}}\delta\omega^2\right)\right] exp(-i\Phi\delta\omega^2)\right\} \\
&\propto \int A(\delta\omega)exp\left(-i\left[\Phi_q - \Phi_f + \frac{\Phi_f^2}{\Phi_f - \Phi_p}\right]\frac{\delta\omega^2}{2}\right)\cdot exp\left(i\frac{\Phi_f}{\Phi_f-\Phi_2}\tau\right)
\end{aligned}
$$

where unified the dispersion of the two pumps becomes an effective $\Phi_f = \left(\frac{1}{\Phi_1} - \frac{1}{\Phi_2}\right)^{-1}$.

The blurring quadratic phase in the inverse Fourier transform integral is removed by setting the phase term to zero. This produces the imaging condition

$$\frac{1}{\Phi_q} - \frac{1}{\Phi_p} = \frac{1}{\Phi_f}$$

that is the imaging condition for parametric time lens, and the dispersion on the pump mirrors the focal length of a spatial lens.

This time-lens can, for example, magnify [43] or compress [44] signals in time.

3.3 Experimental setup

A schematic of the full temporal cloaking device is presented in figure 3.1. A continuous-wave probe beam, which could be used to detect an event, is incident from the left. After passing through the STL the light propagates through a dispersive element (for example, a single-mode fiber) that translates the red and blue parts of the chirped probe to the edges of the time window, creating a temporal gap in the probe beam. Finally, a medium with a dispersion opposite in sign to the previous element (for example, a dispersive-compensating optical fiber), together with a second, similar STL, closes the gap so that neither the occurrence of the event nor the presence of the time-lenses are detected. (We note that the spatial equivalent to this second, negative dispersive element would be one that produces negative diffraction [39] and thus would require a metamaterial with a negative index of refraction.)

The schematical configuration for an all-optical implementation of the temporal cloaking is presented in figure 3.2. We numerically simulated the probe beam as it passes through the system by solving the nonlinear Schrödinger equation. The resulting wavelength of the probe beam as a function of time before and after

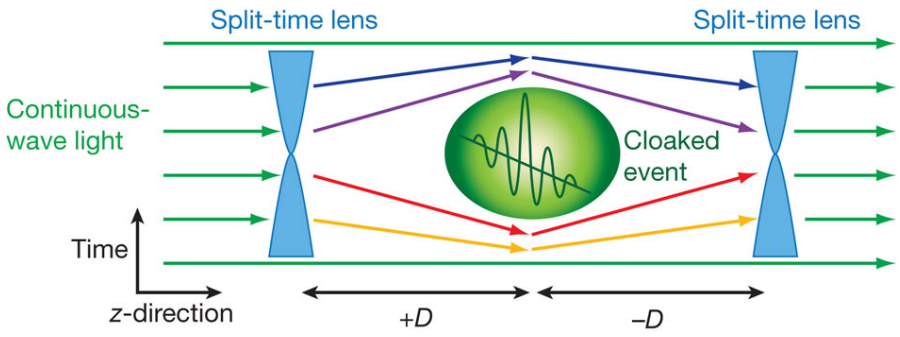

Figure 3.1: Schematics of the temporal cloak using a pair of STLs. Schematics of the temporal cloak using a pair of STLs. The STLs are used to create a temporal 'hole' in a probe beam such that any temporal or spectral changes caused by an event within this hole do not occur. The figure is oriented such that the probe light is described by horizontal lines, and lines at different orientations represent different wavelengths. D denotes the magnitude of the total negative or positive group-velocity dispersion.

the STL is shown in figure 3.2a and b, respectively. The light then propagates through a dispersive element consisting of a single-mode fiber such that the shorter (or longer) wavelengths propagate faster (or slower) than the initial probe beam wavelength. The wavelength distribution as a function of time shown in figure 3.2b becomes that shown in figure 3.2(c), in which a temporal gap opens at the focal point of the STL. The gap is synchronized such that the event occurs within this gap and therefore is not sensed by the probe. The probe then propagates through a dispersion-compensating fiber, and the temporal gap is closed as shown in figure 3.2(d). Finally, a second STL restores the probe light back to its initial wavelength, shown in figure 3.2(e), so that the probe beam is restored to its initial state, and both the event and the presence of the time-lenses are undetected. We note that both after the time-lenses and after the event, we remove the pump from the system with wavelength division multiplexers (WDM).

The split time-lens focuses light to the edges of the time window rather than to the center so that after propagating through a medium with normal GVD, part of

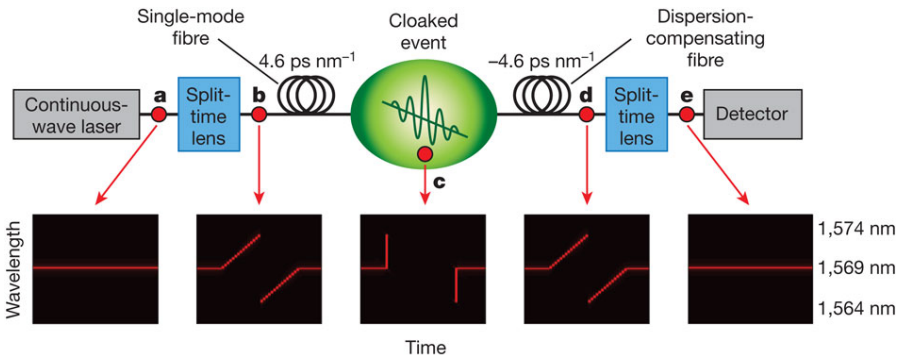

Figure 3.2: Experimental configuration for cloaking an event in time. Top, schematics of the experimental configuration. Bottom, the wavelength of the probe beam as a function of time from numerical simulations. (a), Before the first STL; (b), after the first STL; (c), after propagating through the single-mode fiber; (d), before the second STL; (e), after the second STL. When both STLs are in operation the event is temporally cloaked.

the probe light is delayed in time while the other part is advanced. This is realized by imposing a parabolic phase shift with a discontinuity in the middle as presented in figure 3.3(b).

The full configuration of one STL is presented figure 3.4. A short pulse splits into two paths, each with bandpass filters. One filter has a 0.18 nm bandwidth so that the pulse becomes 20-ps long, while the other has a 10-nm bandwidth so that the pulse duration is shorter than 0.4 ps. figure 3.4(a) presents the wavelength as a function of time for the narrowband pulse and figure 3.4(b) for the broadband pulse. Next, 120 m of single mode fiber (SMF) with a total dispersion of 2.2 ps/nm is exploited to chirp the short pulse into 20-ps long pulse such that the wavelength as a function of time is presented in supplementary figure 3.4(c). Using a diffraction grating we spectrally spread the chirped pulse CW light and reflect the light back into the fiber with two mirrors, one for the longer wavelengths and one for the shorter wavelengths. The two mirrors are displaced by 3 mm so as to obtain a delay of 20 ps between the short wavelengths and the long wavelengths, as presented in figure 3.4(d). Finally, we combine the two pulses, as presented in

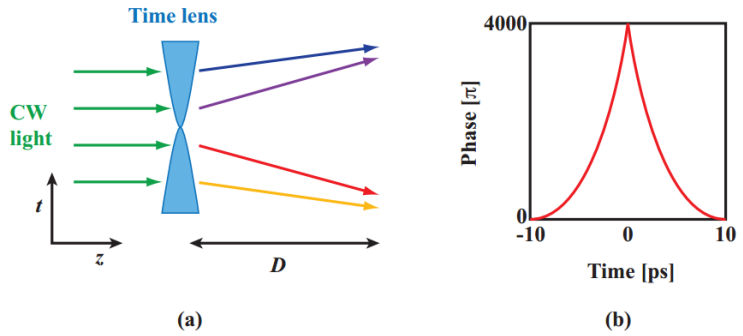

Figure 3.3: Split time-lens (STL) composed of two halves of a regular time-lens which are connected at the tips. Inset (a) presents the space-time schematics of the STL; inset (b) presents the phase as a function of time imposed by the STL.

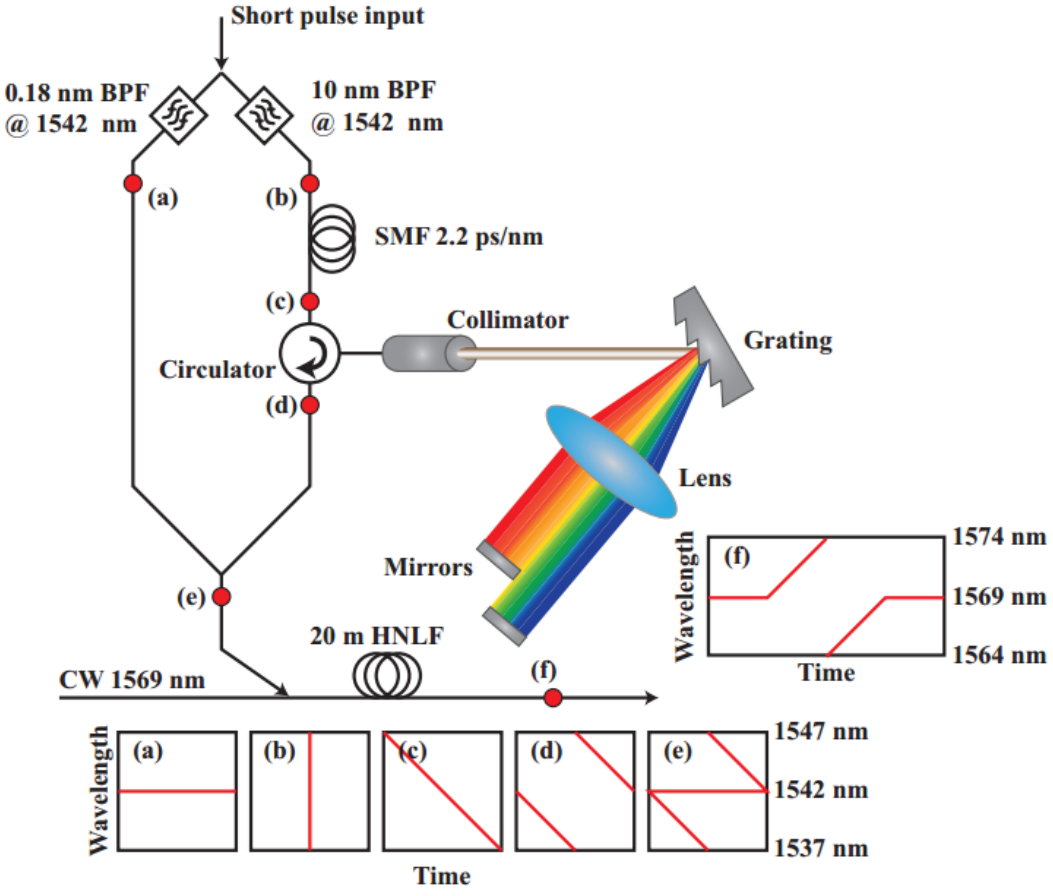

Figure 3.4: Experimental configuration of a single time-lens. Insets (a)-(e) present the wavelength of the pump as a function of time at five different points in the configuration; inset (f) presents the wavelength of the probe beam as a function of time after the split time-lens. BPF - band pass filter; DCF - dispersion compensating fiber; HNLF - highly nonlinear fiber.

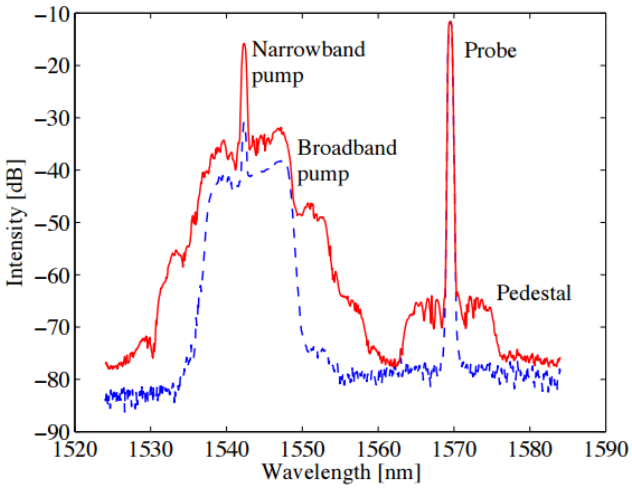

Figure 3.5: The dashed (blue) curve denotes the spectrum of the two pumps and the probe beam before the nonlinear fiber. The solid (red) curve denotes the spectrum after the nonlinear fiber. After the nonlinear fiber, the pedestal around the probe beam is clearly observed, indicating that the wavelength of part of the light from the probe is shifted. We operated the pumps with different power levels such that the two curves will not overlap and will be clearly observed in the figure.

figure 3.4(e). The combined pulses are coupled to the probe laser by a WDMs to serve as pump pulses for the STL. The pump and the probe laser are sent through 20 m of highly nonlinear fiber (HNLF) where the four-wave mixing process between the two pumps and the probe beam shifts the wavelength of the probe beam according to the frequency difference between the two pumps. Therefore, the resulting wavelength as a function of time after the time-lens is linearly spread with a discontinuity in the middle, as presented in supplementary figure 3.4(f). To characterize the STL, we measure the spectrum before and after the nonlinear fiber. The results are presented in figure 3.5. The dashed (blue) curve denotes the spectrum of the two pump beams and the probing light before the nonlinear fiber. The solid (red) curve denotes the spectrum after the nonlinear fiber. The four-wave mixing process transforms part of the light in the probe beam to form a pedestal.

We operate the pumps with different power levels such that the two curves will not overlap and will be clearly observed in the figure. We note that both STLs operate with identical pump pulses and are synchronized. In order for the second STL to completely undo the temporal focusing of the first one, adjustment of the relative phase between the pump waves of the second STL and the signal wave is necessary.

We use a tunable continuous-wave laser (SANTAC TSL-210) to generate the probe wave. To generate the pump waves, we use a femtosecond laser based on an erbium-doped fiber ring laser with a carbon nanotube saturable absorber. Both for the STLs and for the four-wave mixing process used to create the event we use a highly nonlinear single-mode fiber from Optical Fiber Solutions.

3.4 Results

Figure 3.6 shows experimental data illustrating how a temporal gap is created in a probe beam at 1542 nm. Using a tuneable narrow-band filter followed by a fast (30 GHz) photo-detector connected to a sampling scope, we measured the exact time for each wavelength to obtain a spectrogram of the probe beam, after the first STL (blue dots), after the single-mode fiber at the focal length of the STL (red circle), and after the dispersion-compensating fiber before the second STL (green asterisks). After the first STL the probe acquires a frequency chirp, illustrated in figure 3.2b). After the single-mode fiber the higher wavelengths are delayed while the lower wavelengths are advanced so that a temporal gap opens from -25 ps to 25 ps according to figure 3.2c. This gap is closed after the dispersion-compensating fiber, and the frequency chirp returns to that shown in figure 3.2d). Before the first

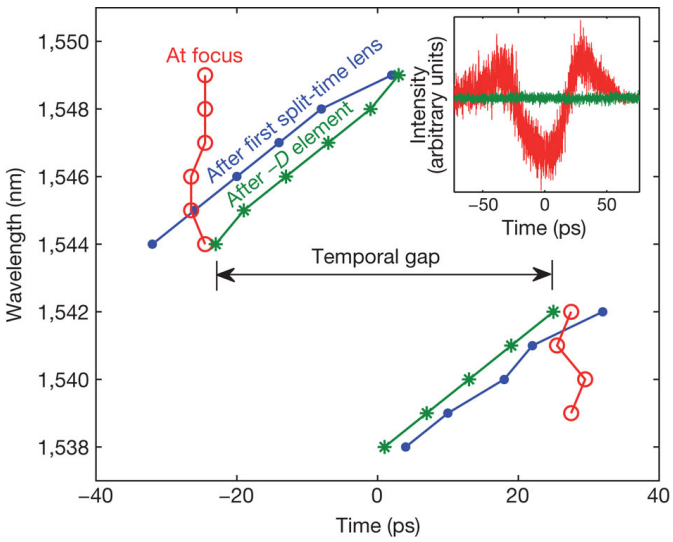

Figure 3.6: Temporal gap in a probe beam. Measured wavelength distribution as a function of time at three locations in the system. After the first STL, the wavelengths are distributed according to figure 3.2b (blue dots). At the focal point, after the positive dispersion element, a temporal gap is opened according to figure 3.2c (red circles). After the negative dispersion element and before the second STL, the gap is closed and the wavelength distribution is returned to its initial state as described by figure 3.2b (green asterisks). Inset, power of the signal as a function of time when the gap is opened (red) and after the gap is closed (green).

STL and after the second STL we detect only the probe at its original wavelength. The inset shows the power of the probe beam as a function of time when the gap is opened (red) and after the gap is closed (green), which provides additional evidence that during the temporal gap the power of the probe beam is significantly lower and that after closing the gap, no appreciable disturbance is observed.

To demonstrate the temporal cloaking capability of this system, we create an event that results in the generation of new frequencies due to the presence of the probe beam. It consists of a nonlinear interaction of a short pump pulse with a probe beam via four-wave mixing with a repetition rate of 41 MHz. When the cloak is off, the probe beam at 1569 nm interacts in a highly nonlinear fiber with a short (5 ps) pump at 1554 nm such that a frequency component is generated at

1539 nm every 24 µs. Thus, the signature of the event is the detection of the 1539 nm signal, and when the cloaking is turned off, it is clearly observed, as shown in figure 3.7a by the dashed (blue) curve. However, when the cloaking is turned on, the amplitude of the detected signal is reduced below the detection noise level, as shown in figure 3.7a (solid red curve) for several interaction events. The spectrum of the output signal in the regime near the idler wavelength is presented in figure 3.7b when the event is uncloaked (blue), when the event is cloaked (red), and without the event (green). To investigate the cloaking efficiency further, in figure 3.7c we present the signal without the event (green) and with the event when the cloaking is off (solid blue curve) and on (red dots) using a highly sensitive detector with a 300-MHz bandwidth. When the cloaking is on, the detected amplitude of the event is more than ten times lower than when the event is uncloaked.

Finally, we investigate the efficiency of the cloak as a function of the pump power of the STLs by measuring the amplitude of the detected event as a function of the pump power used by both STLs. The pump power of the STLs governs the amount of light in the probe beam that is shifted in frequency, so as the pump power increases, less light remains in the probe beam during the temporal gap when the event occurs (see figure 3.8). When the average pump power is 17 mW, the amplitude of the detected signal is 6.1 mV (also shown in the upper inset). As the pump power is increased, the detected amplitude decreases until it reaches the noise level at 2.3 mV (shown in the lower inset), when the pump power of the STL is 37 mW. Increasing the pump power of the STLs further increases the amplitude due to higher pump noise.

Using numerical simulations of the propagation of the signal through our cloaking system, we can predict the output signal amplitude as a function of pump power

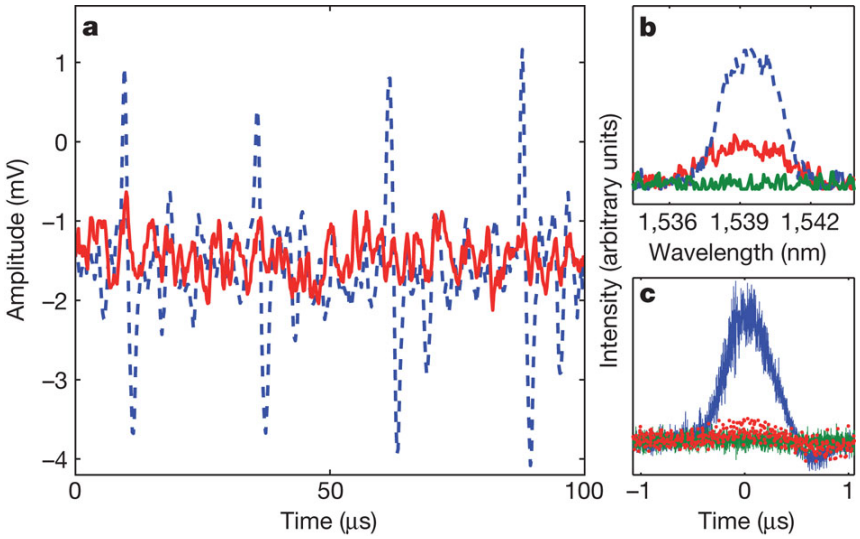

Figure 3.7: Experimental results of the temporal cloaking. Experimental results showing the detection of signal, indicating that the probe beam has undergone an interaction (that is, an event) with a short pump pulse. a, The events occur every 24 μs when the cloaking is turned off (dashed blue curve) and on (solid red curve). When the cloaking is turned on, the amplitude of the signal probing the event is below the detection noise level, indicating that the event has been hidden. b, Spectra of the output signal around 1539 nm as generated from the four-wave-mixing event when the event is uncloaked (blue), when the event is cloaked (red) and without the event (green). c, Temporal measurement of an uncloaked event (blue), cloaked event (red), and without an event (green). The amplitude of the event is more than ten times smaller when the cloaking is on, and the probe beam is nearly identical to that without an event.

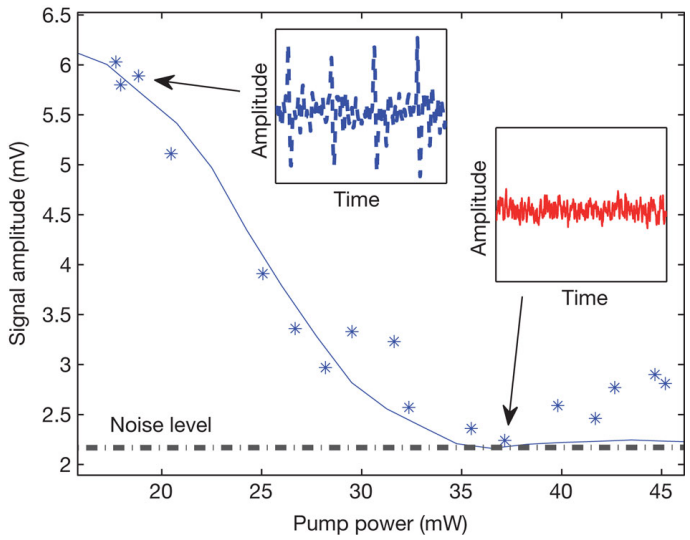

Figure 3.8: Intermediate cloaking. Amplitude of the detected event as a function of the pump power of the STLs. Asterisks show experimental results and the solid curve shows the numerical simulation. The insets show the experimental results of the signal as a function of time when the cloaking is off (upper, blue) and on (lower, red).

for our system. We numerically simulate the STL using the standard nonlinear propagation equation with dispersion under the slowly varying envelope approximation.

We model the pump field $E_p(t)$ as the sum of a short CW field and a rectangularly dispersed pulse. The dispersed pulse is calculated by multiplying the FFT array with the dispersion operator $exp(i\Phi\omega^2)$. Half of the spectrum of the pump is then delayed with respect to the other to create the split time-lens. Next, we obtain the time-lens process by multiplying a constant probe with $exp(i\gamma|E_p(t)|^2)$, and propagating the probe through the dispersive material such that the dispersion operator $exp(iD\omega^2)$ is applied on the resulting field. To simulate the event, we solve the nonlinear interaction between the probe at the focus and a short pulse of light. The result from this interaction yields the perturbed field that is used to detect the event. To obtain the amplitude of the perturbed field as a function of

the pump power (figure 3.8 solid curve), we perform the simulation for different values of γ, i.e. different pump power and took into account the noise level of the detector. We also calculate the spectrogram of the probe beam before and after the first STL, at the focus, and before and after the second STL.

The results are shown as the solid blue curve in figure 3.8 and show good agreement with the experimental results.

The temporal gap can be readily widened by increasing the dispersive broadening of the pump and the dispersion between the STLs. However, as the dispersion is increased, effects due to third-order dispersion arise, which will prevent the gap from closing completely unless the third-order dispersion is compensated. In our experiment, the spectral and temporal width of the pump pulses before chirping are9 mm and 0.4 ps, respectively, which results in third-order dispersion limiting the width of the temporal gap to 110 ps, as long as the pump power is increased to efficiently deplete the probe beam completely within the gap. Nevertheless, given that the third-order dispersion is proportional to $\Delta\omega^3$ whereas the amount of linear frequency chirp is proportional to $\Delta\omega^2$ [45], it is possible to increase the temporal gap by resorting to narrower pump pulses and introducing more dispersion. The limitation in this case is stimulated Brillouin scattering, which limits the length of the single-mode fiber to 50 km and the temporal gap to a width of a few nanoseconds.

3.5 Conclusions

In summary, we have presented the first experimental demonstration of temporal cloaking that successfully hides an event from a probe beam in the time domain

[37]. Our scheme is based on the space–time duality, using a pair of STLs. The STLs use parametric four-wave mixing such that dispersion manipulation is highly efficient, and can readily be adapted for other wavelengths in the electromagnetic spectrum. Our results represent a significant step towards obtaining a complete spatio-temporal cloaking device. Following our work an EOM-based implementation was demonstrated [46, 47].

Our results could find application beyond full spatial temporal cloaking. Although spatial cloaking is still limited in angular acceptance, wavelength, polarization and efficiency, we have shown that we can deplete a probe wave and restore it to its original state after the event. This suggests it is possible to use similar technology for routing different optical data streams coming simultaneously into a single optical data processing unit by opening a gap in one of the data streams and restoring it to a different time so that it will arrive after the other stream has been processed[48].

CHAPTER 4

LOW-NOISE BRAGG SCATTERING AT THE QUANTUM LEVEL

The creation of a scalable quantum-enabled machine, e.g. a quantum computer or a quantum communication system, requires the development of many elements, such as sources, memories, processing elements, measurement devices and a network able to inter-connect different resources [49, 50]. Optical connections are indeed good candidates for the transmission of quantum information, in the form of *flying qubits*, single photons, or other nonclassical states, that can travel undisturbed over long distance. The major obstacle to such scheme is that often different elements work at different wavelengths: in some cases because implementations are constrained to certain wavelength ranges, e.g. atomic resonances used for quantum systems are often in the visible or very near infrared, while the transmission window of fiber is in the 1300 nm - 1600 nm bandwidth; in other cases because working with similar, but not identical, resonant elements requires finetuning of the frequency, e.g. GaAs quantum dots emitters present variation in their energy levels due to differences in the mechanical strain.

With the goal of creating a tunable nonclassical light source, frequency translation was first proposed in 1990 [10] and observed two years later [51]: one beam of a squeezed twin beam was converted from the original 1064 nm to 532 nm using parametric up-conversion in KTP crystal, and nonclassical correlations were

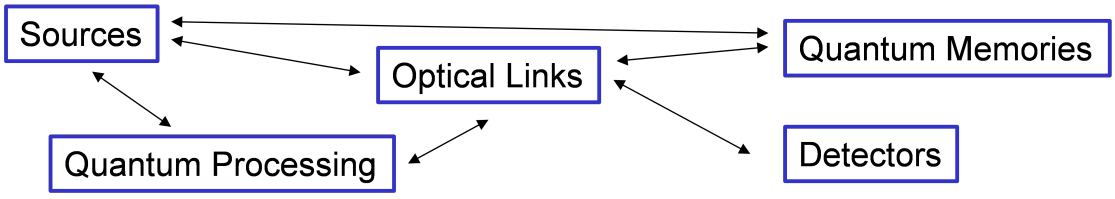

Figure 4.1: A quantum architecture

preserved in the conversion.

Later on, single photons were translated from 1550 nm to 780 nm using periodically poled lithium niobate (PPLN) crystal and detected with silicon single photon detectors, rather than less-performing InGaAs operating in the near infrared, thus increasing the overall detection efficiency [52, 53, 54]. Other demonstrations showed high efficiency [53, 55], preservation of quantum coherence [56] and entanglement [57]n and the ability of interfacing different sources, by removing frequency distinguishability [58]. In 2005, it was noticed that among parametric $\chi^{(3)}$processes, Bragg Scattering can frequency translate quantum states without adding parametric noise [59]. Follow up realizations include photonic crystal fiber [59], highly nonlinear fiber [60] and both SiN waveguides [**?**] and resonators [17]. Other approaches to quantum frequency translation include cross-phase modulation [61, 62], opto-mechanical hybrid systems [63, 64], electro-optical modulation [65], Alkali-vapor cells [66], and microwave superconductor resonators [67].

In the last few years, frequency translation has emerged as a mean to directly manipulate quantum in the full temporal and spectral space: by tailoring the pump spectrum and using concepts borrowed from parametric time-lens, both temporal compression [68] and magnification [69] of quantum states can be implemented. While using temporally-shaped pump it is possible to select and convert different temporal modes , realizing a optical pulse gate [70].

Both $\chi^{(2)}$ and $\chi^{(3)}$ implementation have to grapple with technical noise, usually generated by the strong pump driving the nonlinear process. In the case of the former implementation conversion efficiency close to 100 % with limited residual noise is routinely obtained, however, for the latter, conversion at unitary efficiency was only obtained at the expenses of a signal polluted by large Raman noise [71] .

4.1 Parameter choice

An optimal choice of nonlinear medium and operating regime enables BS frequency translation in the quantum regime. There are two major design decisions that affect the choice of medium. First, one must fulfill the phase matching for a given set of pumps and signals. In fact, given the selectivity of the process, a very specific dispersion profile must be used for any given configuration. Dispersion of the nonlinear medium determined the work regime in previous demonstrations: both pumps and signal in the 1550 nm range in highly nonlinear fibers [60, 71, 72], pumps at 820 nm, signals at 630 nm in photonic crystal fiber [73], pumps at 1550 nm and signal at 980 nm in SiN waveguides [74]. The second design decision is the balance between nonlinearity and dispersion properties: an optimal ratio between the amount of pump power required for full conversion and the acceptance bandwidth, as well as the minimum frequency separation $\Delta\omega$ for which cascaded BS becomes prominent. In order to maximize the former with respect to the latter, it is convenient to work at large dispersion values $\beta^{(2)}(\omega_s) \simeq \beta^{(3)}\Delta\Omega$, or work with large frequency separation. As a reference, the demonstrations reported above showed translation over $\Delta\omega > 10$ nm

As mentioned in the introduction, one obstacle for most quantum implementation of BS is technical noise, in the form of spontaneous FWM and Raman noise. In figure 4.2 we show that they spectrally contribute when generated by a strong pump sitting at 1560 nm.

Modulation instability (purple in figure 4.2) is a competing FWM process, its gain profile given by

$$G_{MI} = 1 + \left(\frac{\gamma P_0}{g_{mi}}\right)^2 \sinh^2(g_{mi} z)$$

where

$$g_{mi} = \sqrt{(\gamma P_0)^2 - (\kappa_{mi} + \gamma P_0)^2}$$

and

$$\kappa_{mi} = \left[\beta(\omega_p + \delta\omega) + \beta(\omega_p - \delta\omega) - 2\beta(\omega_p)\right]/2$$

is the linear phase mismatch for a frequency detuning $\delta\omega$ from the pump.

Modulation instability affects BS in multiple ways, either by depleting the pump and generating spurious sidebands, or amplifying the vacuum fluctuations and generating pairs of energy correlated photons. It can be managed placing the pump on the normal dispersion, where parametric gain is forbidden and the bandwidth for pair generation is minimized. We also notice that G_{MI} decays very fast with detuning.

Spontaneous and Stimulated Raman Scattering are processes that couple light with the thermal phonons of the medium. Scattering strength depends on the density of occupied states as well as the Raman spectrum $g(\delta\omega)$. The probability of a spontaneous Stokes scattering (i.e. the photon losing energy) is given by

$$p_S(\delta\omega) = g(\delta\omega)\frac{1}{1 - exp(-\delta\omega\hbar/kT)}$$

while for anti-Stokes it is

$$p_{aS}(\delta\omega) = g(\delta\omega)\frac{exp(-\delta\omega\hbar/kT)}{1 - exp(-\delta\omega\hbar/kT)}$$

The spectrum depends on the material: amorphous materials have a broad spectrum (i.e. for glass it extends to about 40 THz [75]), while crystalline materials have strong, sharp features. Both processes become less probable for very large detuning, though the anti-Stoke probability depends exponentially on the

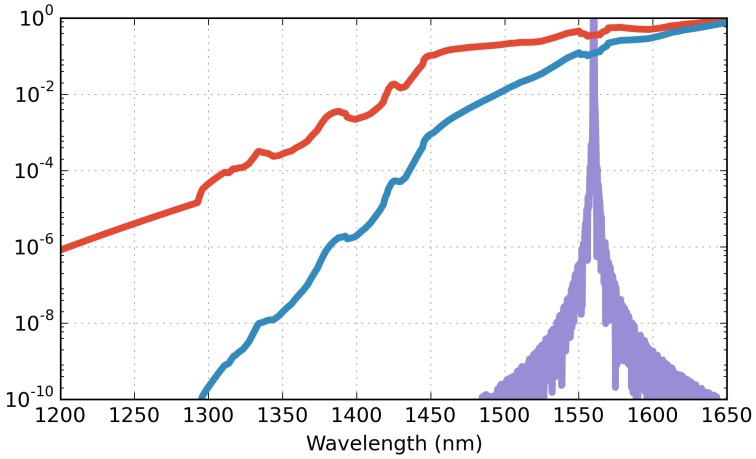

Figure 4.2: Technical noise contributions to BS for large detuning. Spontaneus pairs generation (purple) . Spontaneus Raman scattering at room temperature (red) and at 76 K (blue)

temperature when $\delta\omega \gg kT/\hbar$ (6 THz for room temperature), so that cooling the fiber can further reduce the noise by several order of magnitude (red 300 K and blue 90 K on figure 4.2) [76, 77].

Thanks to the BS phasematching selectivity, there are no limitations on the amount of detuning $\Delta\Omega$ [78] between pumps and signal, the only fundamental parameter being ω_{ZDW} (rather then $\beta^{(3)}$), easily tunable via dispersion engineering.

We operate using a dispersion shifted fiber Vistacor from Corning inc.. Although the fiber is not optimized for nonlinear interactions ($\gamma \approx$3 W/km), a sufficiently long spool makes up for the reduced nonlinear parameter. Measurement of the dispersion measures $D(\lambda) = 3.52{\cdot}10^{-4}(\lambda - \lambda_{ZDW}) - 2.75{\cdot}10^{-7}(\lambda - \lambda_{ZDW})^2 \frac{ns}{nm\,km}$ with $\lambda_{ZDW} = 1420\,nm$ that corresponds to a $\omega_{ZDW} = 1330\,THz$,$\beta^{(3)} = 7.7 \times 10^{-2}\,\mathrm{ps}^3/\mathrm{km}$, $\beta^{(4)} = 2.28 \times 10^{-4}\,\mathrm{ps}^4/\mathrm{km}$ (figure 4.3), optimally placed between two telecommunication windows, the O-Band (1260 nm, 1340 nm) and the C-Band (1530 nm - 1565 nm) $\Delta\Omega \approx 120THz$. This is an attractive configuration because it enables the large detuning needed for a low-noise operation, while still operating

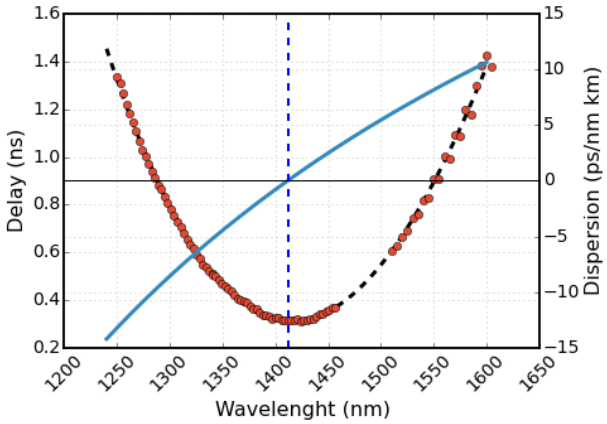

Figure 4.3: Vistacor dispersion

at wavelengths where off-the-shelf equipment is available. For $\Delta\omega = 5THz$ (about 6.5 nm at 1560 nm and 4.3 nm at 1300 nm) the acceptance bandwidth is $\delta\omega_{bs} = 1/L\beta^{(3)}\Delta\Omega\Delta\omega \approx 22\,\mathrm{GHz\,km^{-1}}$ ($79\,\mathrm{GHz\,km^{-1}}$ FWHM). We also notice a large contribution of $\beta^{(4)}$ that determines a shift to the optimal wavelength of $\Delta\epsilon \approx 12\,\mathrm{THz}$ (independently of L)

During this work, we used different sections collected from the same spool of fiber, and we notice variations in the optimal conversion frequency up to 0.2 nm. This is due to fluctuations of the core diameter and the high selectivity of the phasematching.

4.2 Experimental Setup

The typical experimental setup is shown in figure 4.4.

To generate pump fields we use two kind of sources. In the original setup we use two CW tunable lasers (Agilent) that were amplitude modulated via EOM. In an updated version of the setup, we use temperature stabilized laser diode

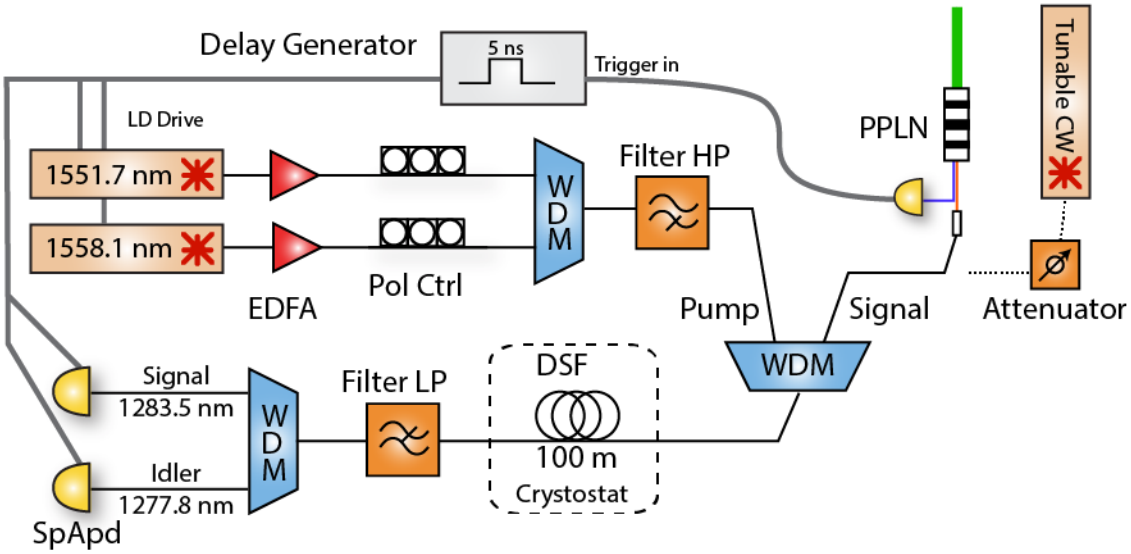

Figure 4.4: Typical Bragg Scattering setup.

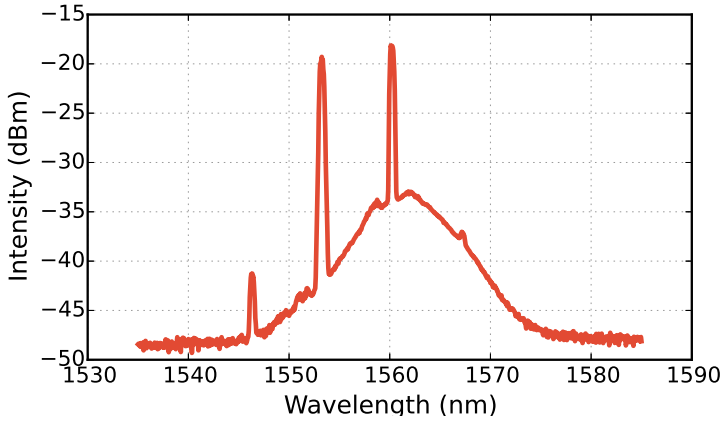

Figure 4.5: Typical pump spectrum (after the nonlinear interaction).

(Qphotonics) that are current modulated via a pulse generator. In both cases pump lasers generate pulses of duration τ =1-10 ns and peak power 5 mW. The pumps are amplified with cascaded c-band erbium-doped fiber amplifier (EDFA). The last EDFA (Keopsys) is optimized for high power pulsed amplification at low duty cycle (output P_{out} = 30 dBm at 100/1 duty cycle). The reason of the change is that it was hard to difficult to generate the required power due to saturation of the EDFA, because of the large amplification and low dutycycle, even with DC extinction close to 30 dBm,

Both pulses are temporally separated when traversing the EDFA to avoid mutual nonlinear effects in the gain medium, and synchronized afterward using an unbalance combination of 1551.7 nm fiber wavelength division multiplexers (WDM).

A free space filtering setup removes higher frequency noise (low-pass filter, cut-off 1550 nm) and selects one polarization with a combination of $\lambda/2$- and $\lambda/4$- waveplates, and a polarizing beam splitter. Signal and pumps are coupled together using O-Band/C-band WDM, temporally synchronized and injected in the nonlinear fiber. At the end of the interaction, second WDM removes most of the pumps, and the signal is sent to the detection stage.

The 100 m of nonlinear fiber is spooled and placed in a Styrofoam box that operates as a cryostat. Signal losses through the setup are as low as 2.6 dB, due to splices, connectors and WDMs. Since the second WDM removes $>$ 30dbB of pump power, we consider most of the Raman noise generated between the two WDMs, and we take care of placing as much amount of fiber as possible in the cryostat.

Before detection, the signal has to be carefully filtered of all residual pump photons and thermal noise: while the pump could be rejected purely via fiber-based

component, it is technically harder to remove the broadband noise between the two optical bands (1360 nm - 1480 nm) that is generated by Raman scattering. To ensure adequate filtration we used a combination of a fiber-based 1300 nm/1550 nm pass/reject filter and a free-space filtering setup (3 dB losses) composed of a lowpass sharp-edge filter (1300-Semrock). A fiber-based WDM (passband 1290 ± 6.5 nm nominal) can be used to separate the signal and idler fields at approximately 1283.3 nm and 1278.5 nm. For some of the measurements, we selected a narrow band (0.5 nm) using a grating filter (2.6 dB), or we used a Dispersion Compensating Module (DCM $D = -1200\, nm/km$ at 1300 nm, 7.6 dB losses) for spectral characterization using time of arrival information to recover the wavelength.

For detection, we use homebrew InGaAs single photon detectors in gated configuration. The diodes (Princeton Lightwave) are cooled to $-40\,^{\circ}$C with thermoelectric coolers to reduces dark counts. (q.e. = 15 %, gate duration = 20-60 ns, rep rate $\leq$ 100 KHz). The gate signal is generated from the same delay generator that provides the pump current pulses.

Temporal measurements are performed using a Time Tagging Module (TTM) with internal resolution 86 ps, capable of operating over 8 channels. The time delay between triggering and detection is about 1200 ns.

A tunable laser (1260 nm-1340 nm) is used both for testing purposes and, in combination with a tunable attenuator, to generate a weak coherent pulse. This laser can be modulated via electro-optical modulation or used in CW configuration.

To generate single photons we use a source based on spontaneus parametric downconversion in PPLN crystal . In a 10 mm crystal, phasematching is achieved via temperature tuning, a CW pump at 543 nm generates photon pairs: 940-nm

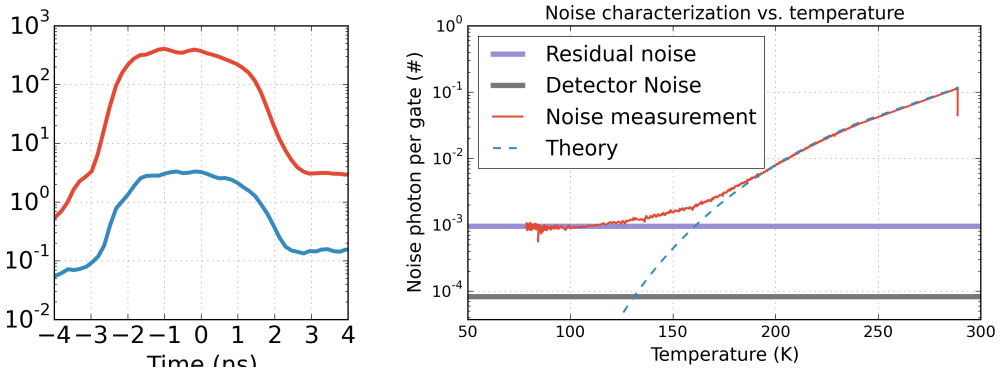

Figure 4.6: Characterization of the noise dependency on temperature (a) Noise (cps) from 4 ns long pump pulse, at at full conversion pump power as detected on one APD for room temperature (red) and 77 K (blue). (b) Total noise photon generated vs. temperature.

photons are detected by a Si APD to herald the presence of 1283-nm photons and generate a synchronization signal that is used trigger the pulse generator. The marginal bandwidth of the signal photons is larger $>$ 10 nm, The heralding photons are filtered with a grating to match signal photon to the acceptance bandwith of BS-FWM, (unless stated, at 1283.8 with 0.5 nm FWHM). An heralding signal of approx. 67 kcps is observed, with a probability $P_{cc} = 5\,\%$ of coincidence detection of the heralded 1283.5 nm photon.

We monitor the noise at one of the outputs while the fiber is changing temperature. If we collect the full signal setup, where contributions come over 12 nm bandwidth of the WDM, we can observe the temperature dependency (figure 4.6). The reduction of noise is limited to 2 orders of magnitude, which is expected because of the amount of fiber not placed in the cryostat (about 1 meter over 100 m of fiber in the cooler).

Taking losses into account, we calculate the probability of generating a photon of noise is $P = 1 \times 10^{-3}$, while being already extremely low compared with other BS demonstrations (P =1 per gate in highest efficiency reported [71]) can

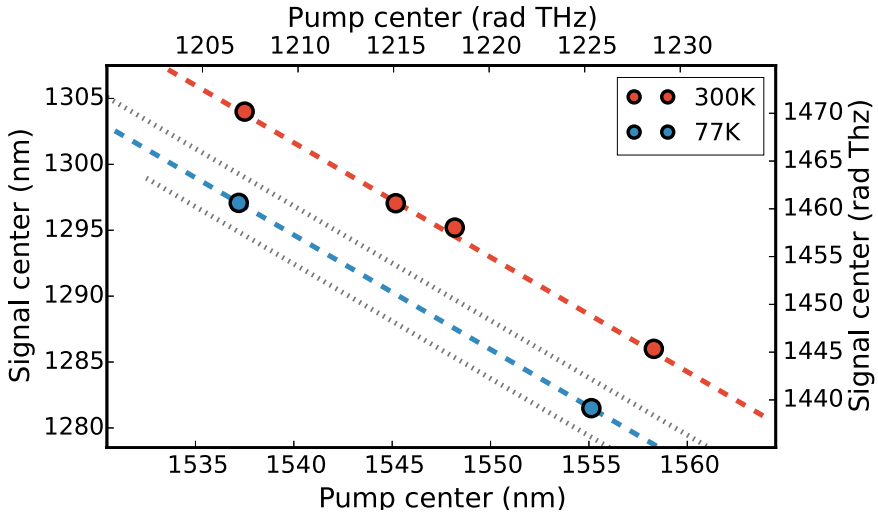

Figure 4.7: Measured phase matching for different $\Delta\Omega$ at 300 K and 77 K. Because of $\beta^{(4)}$ and cooling contribution, optimal signal frequency is shifted by 20.5 THz from the value expected from our characterization of $\beta^{(3)}$ at room temperature.

be additionally filtered both temporally and spectrally to match the acceptance bandwidth.

4.3 Frequency Translation

We characterize the system by performing experiments at room temperature and at cryogenic temperature for different pump settings. In figure 4.7 we summarize the optimal conversion wavelength at different temperatures, as we change $\Delta\Omega$. When cooled with liquid nitrogen, the optimal conversion frequency changes because of dispersion modification due to the thermal expansion. We extract the $\beta^{(4)}$ contribution, which shifts the optimal signal frequency by $\Delta\epsilon = 20.5$ THz for $\Delta\Omega$ =118 THz

For a fixed set of pump wavelengths, we scan the signal field and reconstruct the phasematching curve. For $\lambda_{p1} = 1551.7$ nm and $\lambda_{p2} = 1558.6$ nm it is shown in

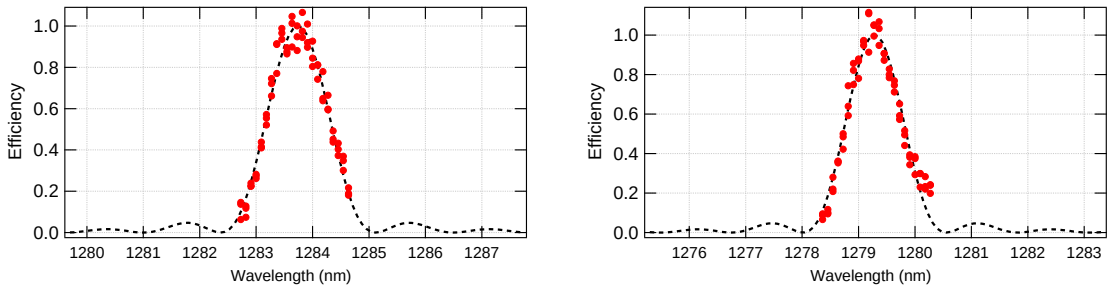

Figure 4.8: Measured acceptance bandwidth of BS process: (left) up-conversion, (right) down-conversion. In dashed line, the fit to give $\delta\lambda_{BS} = 1.17(2)$ nm FWHM ($\delta\omega_{bs}$ =1.35 THz)

figure 4.8. Sending a CW signal, we observe depletion on the CW background and creation of a idler pulse. As expected, the upconversion and the downconversion are reciprocal.

For this pump configuration, we measure perfect phasematching for λ_s =1283.74(5) nm and λ_i =1279.28(5) nm. We tune our CW source at λ_s, attenuated to a level of less than one photon per gate , and measure the conversion efficiency η as the total pump power varies, while keeping the two pumps balanced and the polarization aligned.

We tune the single photon source to emit an heralded photon at λ_s into the BS setup. When the pump is temporally overlapped, we observe depletion and conversion. In figure 4.10 we observe the detected trace on the APD for increasing pump power. To obtain this curve, signal and idler are separated in the freespace setup and each one filtered with a 0.5 nm filter (signal 3 dB losses, idler 6 dB). We show the conversion curve in figure 4.10.

Without filtering the conversion efficiency is limited by the fact that single photon bandwidth ($\delta\lambda$ = 0.57 nm FWHM) and the acceptance ($\delta\lambda_{BS} = 1.17(2)$ nm FWHM $\delta\omega_{bs}$ =1.35 THz) are comparable. In figure 4.9 we plot the theoretical

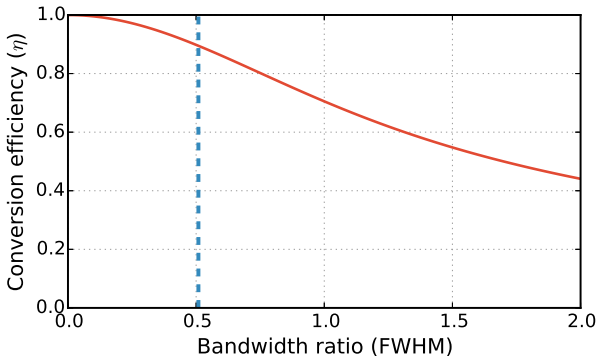

Figure 4.9: Efficiency vs. signal over acceptance bandwidth ratio $\delta\omega/\delta\omega_{bs}$. In blue we highlight the condition of our experiment, for a ratio $\delta\omega/\delta\omega_{bs}$ =0.51 we expect a conversion efficiency η =89 %.

calculation of translation efficiency, and we obtain a theoretical maximum efficiency of about 89 %

We measure the second order correlation of the output state to verify the preservation of the quantum statistic on the translated output. We inject the output field into a 50/50 fiber beamsplitter, and record detection rates $A(t)$ and $B(t)$, and coincidence rate $C(\tau)$ from the two coupler outputs. Normalization of the $g^{(2)}(\tau) = C(\tau)/N(\tau)$ is obtained from the discrete cross-correlation of the singles $N(\tau) = A(t) * B(t)$. Error bars are extracted from statistical error on the count events. To remove the dark counts contribution to the measurement, we observe that the contribution of the dark counts to the coincidence count is (with the assumption of uncorrelated noise) $C_{dc}(\tau) = A_{dc}(t)*\bar{B}(t)+\bar{A}(t)*B_{dc}(t)+A_{dc}(t)*B_{dc}(t)$, where $A(t) = \bar{A}(t) + A_{dc}(t)$ and $B(t) = \bar{B}(t) + B_{dc}(t)$.

We compare the $g^{(2)}(\tau)$ measurements of the single photon traversing the setup, with pump either off of on. Even if the fields are not selected, because of the large conversion efficiency, we are measuring respectively at λ_s and λ_i: we observe an input (i.e. converted) $g^{(2)}(0)$ =0.19. Though this value is below 0.5, the non

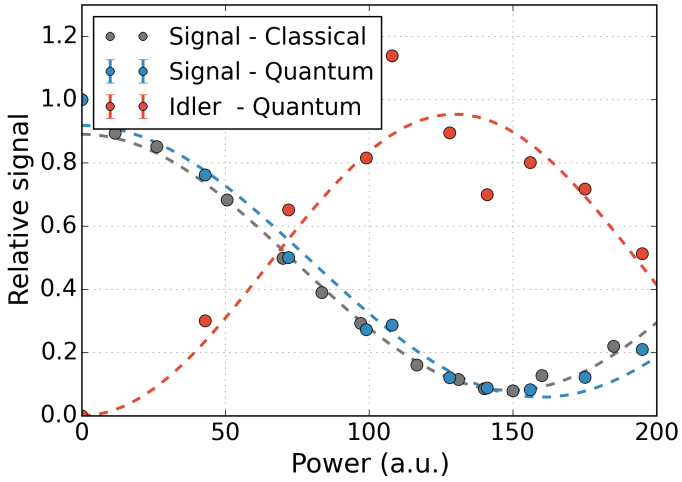

Figure 4.10: Frequency translation efficiency vs pump power for a weak coherent state and for single photon. From a fit we extract a translation efficiency of η =94(1) %

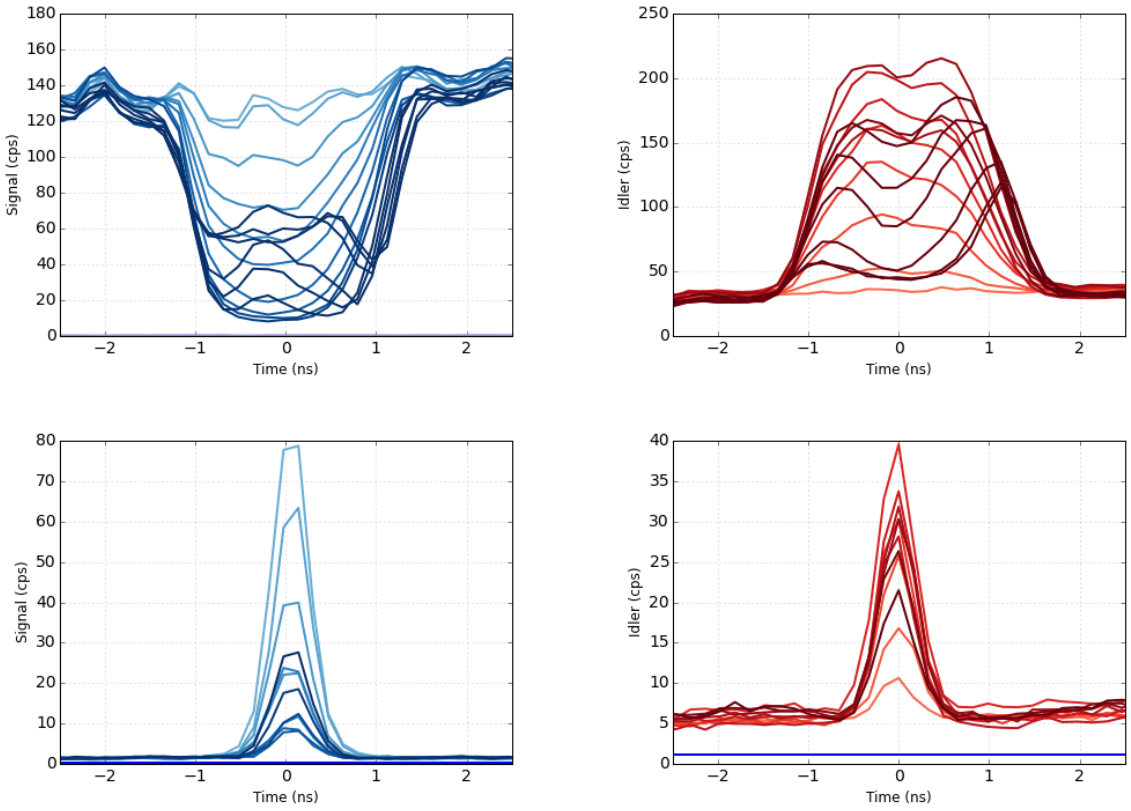

Figure 4.11: Traces of signal (left) and idler (right) field for increasing pump power. (top) Weak coherent state. (bottom) Single photon.

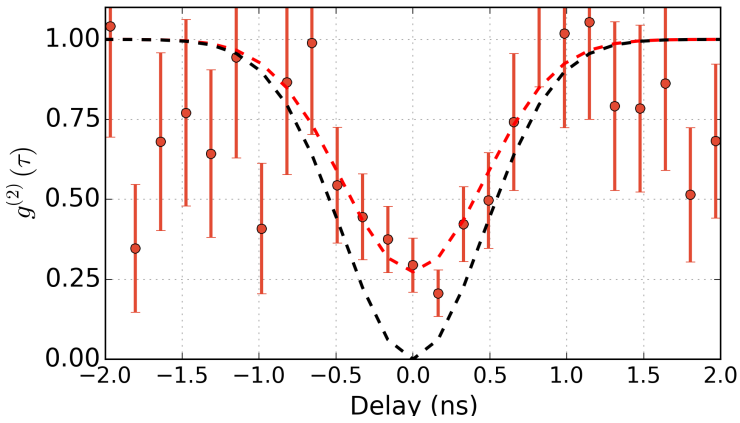

Figure 4.12: $g^{(2)}(\tau)$ measurement of filtered idler: $g^{(2)}(0)$ =0.2(1) . When we correct for dark counts, we obtain $g^{(2)}(0)$ =0.02(2).

classical boundary for single photons, it is limited by the presence of generated photons at $\lambda \neq \lambda_s$ that are not heralded but create a background noise. Upon frequency translation, the correlation takes the value of $g^{(2)}(0) = 0.23$, showing a slight increase but still well within the quantum regime.

Next, we select the idler field with the free space filter and repeat the measurement, shown in figure 4.12: fitting the raw data with a Gaussian factor, we measure $g^{(2)}(0)$ =0.2(1) (the losses introduced by the filtering reduced the SNR). When we correct for dark counts, we obtain $g^{(2)}(0)$ =0.02(2). Because of $g^{(2)}(0)$ is a bounded number, we utilize Bayes statistics to estimate the uncertainty.

4.4 Quantum time lens

Frequency translation, as we have seen in 3.2, provides a way to modulate via frequency mixing of the pumps with the signal, and among the many applications it is possible to coherently modify the spectral properties of a quantum state, for example compressing and expanding its spectrum. This fact holds true for

quantum frequency translation as well [79].

One important rationale is juxtaposition between narrowband and broadband systems: on one hand, probabilistic sources of broadband single photons $\delta\nu \gg 100$ GHz, as achieved by parametric downconversion, are currently commonly used for their brightness and ease of construction. Moreover, their high timing resolution and strong spectral correlations being a resource for quantum experiments. On the other hand, intrinsically optically narrowband systems $\delta\nu \ll 100$ MHz , e.g. atomic transitions or optomechanical cavities, show the promising prospect of implementing several elements needed by a "quantum architecture", such as memories and gates [50, 80]. While it is always possible to filter the source to match the target bandwidth, doing so drastically reduces the efficiency of the source (we have a direct example in our quantum source). A better route is to place the source into a resonant cavity [81, 82] or use a narrowband source based on atomic single or ensemble emitters [83, 84, 85]. Even with such sources, one would still need the ability to tune exactly into a system, both in its central frequency and in the shape of its spectrum [68]. Optical manipulation of the spectrum enables an efficient way to tune and optimize any kind of quantum optical system, bridging the gap between two widely different regimes.

Other applications are inspired by nonlinear optics signal processing and time-space duality, as already described in section 3.2. For example, temporal magnification can be used to overcome the limited temporal resolution of single photon detectors when characterizing time-bin entanglement and polarization entanglement [86, 87] for single photons with short coherence time, or pairs with short correlation time. Another application is conversion between different temporal-frequency modes, as a way to achieve large multiplexing and extending detection

capabilities [70].

In general, achieving frequency translation using broadband pulses while retaining full conversion is a complex problem [88, 89]: temporal features of the pump affect the efficiency of the conversion (heuristically for different instant τ the conversion efficiency varies). Also the bandwidth of the fields may be comparable with the bandwidth of the phase matching. Optimization of the process may require nontrivial shaping of the pump fields and, for certain applications, such as sorting orthogonal temporal modes [90], perfect efficiency is theoretical not achievable.

In our experiments, we operate in a regime where these conditions can be relaxed: firstly, all the broadband fields are linearly chirped to the limit of large dispersion $\Phi^2\delta\omega^4 \gg 1$ (where $\Phi = \beta^{(2)}L$ is the linear chirp and $\delta\omega$ is the pulse bandwidth), so that a broadband pulse at the interaction is chirped, i.e. there is a 1 to 1 correspondence between time and frequency (i.e. $\omega \to \omega(\tau) \propto \tau/\Phi$). This is common condition for time-lens setup [8]: one can rewrite the frequency conversion BS equation (2.4) where the frequency

$$a_i(\tau, z) = -i\frac{e(\tau)}{k_{bs}(\tau)}\sin\left[k_{bs}(\tau)z\right]a_s(\tau, 0)$$

gain $e(\tau)$, and the phasematching $\kappa(\tau)$ are well defined for each instant τ. The idler field is then defined by $a_i = \int a_i(\tau)e^{i(\omega_s(\tau)+\omega_{p1}(\tau)-\omega_{p2}(\tau))t}d\tau$ where the exponential terms account for final energy conversion. For $\kappa(\tau) = \kappa$, it reduces to the general case described when deriving time-lens expression.

Let's expand $\kappa(\tau)$ for broadband pulse: we assume that the 4 fields are centered at the phasematched condition $\omega_{s,p1,p2} = \bar{\omega}_{s,p1,p2} + \delta\omega(\tau)_{s,p1,p2}$ ($\kappa|_{\bar{\omega}} = 0$, with

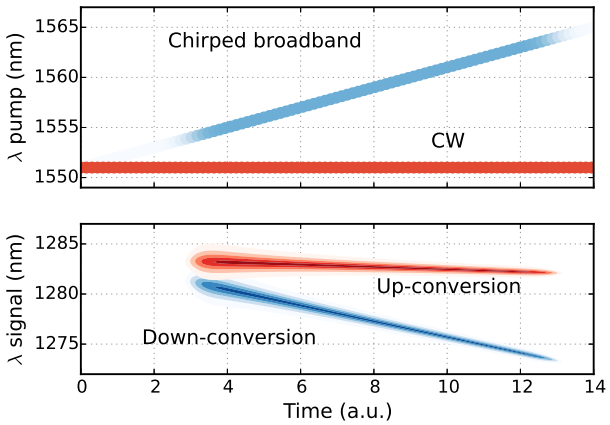

Figure 4.13: Theoretical phasematching for a time-lens asymmetric configuration (top): a chirped pump (blue) and a quasi CW pump (red) . The x-axis shows an arbitrary time scale. (bottom) Phasematching curve: the optimal wavelength 'shadows' the pump temporal-spectral distribution.

conditions, obtained in chapter 2, $(\bar{\omega}_{p2} - \bar{\omega}_{p1})/2 = \omega_{ZDW} + \Delta\Omega_p$, $\bar{\omega}_s = \bar{\omega}_{DZW} - \Delta\Omega + \Delta\omega/2 + \Delta\epsilon$). With the assumption of $\Delta\Omega \gg \delta\omega$, the phasematching condition becomes

$$\kappa(\tau)L \simeq \beta^{(2)} L\Delta\Omega \left[\Delta\omega + \delta\omega_{p1}(\tau) - \delta\omega_{p2}(\tau)\right] \left[\delta\omega_s(\tau) + \delta\omega_{p2}(\tau)\right]$$
$$\simeq \left(\delta\omega_s(\tau) + \delta\omega_{p2}(\tau)\right) / \delta\omega_{bs}$$

where we recognize the acceptance bandwidth $\delta\omega_{bs} = \Delta\omega/\delta k_{bs} L$.

Indeed we find trivial the case when bandwidth is smaller than the acceptance, the phasematching is always fulfilled. The interesting case is when $\delta\omega_s(\tau) = -\delta\omega_{p2}(\tau)$, i.e. $\Phi_s = -\Phi_{p2}$, that implies a broadband conversion: from the energy conservation, the idler will be $\delta\omega_i(\tau) = \delta\omega_s(\tau) + \bar{\omega}_i$.

We visualize such a condition in figure 4.13. A given pair of pumps chirped in time (x-axis), shown on the top of the plot, determines a region in the spectrum where conversion is allowed by phasematching (upconversion in blue, downconversion in red) that is the "shadow" of the chirped pump: as the signal overlap

with one of the shadows, it will fully be converted to the other shadow. The total bandwidth of the interaction can be much larger than the acceptance bandwidth.

From the previous derivation in section 3.2 we obtained that the focal properties of a BS time-lens is $\Phi_f = (1/\Phi_{p1} - 1/\Phi_{p2})^{-1}$. Since the phasematching condition constrains the only one of the pumps, we can use the freedom of Φ_{p1} to realize any time-lens of focal Φ_f. It is a feature, derived from the additional degree of freedom that the second pump introduce, that sets BS apart from $\chi^{(2)}$ systems. In the latter, the condition for unitary efficiency under chirped signal and pumps are stronger [89]. Demonstration [87] provides the record for spectral compression with an internal efficiency 0.3 %.

One special case is for one pump being a monochromatic pulse with duration longer than the dispersed broadband pump: for that, $1/\Phi_p \to 0$ and $\Phi_s = \Phi_f$. In the time-lens paradigm, it corresponds to imaging from (or at) a distance equal to the focal length. This is the limit to large magnification $M \gg 1$ (large compression $M \ll 1$), and can also be seen as the Fourier transform limit, because it converts time to frequency and reversal.

4.4.1 Temporal compression

The setup is very similar to the one presented in section 4.2, with the following modifications:

One of the pump diode lasers (the one at 1558.3 nm) is substituted with a homebrew passive modelocked femtosecond fiber laser that acts as a broadband pump (similar to our temporal cloaking setup).

This laser has a repetition rate of 50 MHz and a soliton spectrum of FWHM $\approx$ 6 nm. The pulse is broadened via modulation instability in a nonlinear fiber to obtain a flat spectrum across $>$ 4 nm (figure 4.14 left) . The repetition rate of the pump is lowered to 100 kHz using a EOM to carve only one pulse every 10 µs. Low duty cycle is needed to reduce the average pump power requirement. A pulse pickup is used to trigger the system, synchronizing the 1551.7 nm pump, the signal and the detectors. The broad pulse is dispersed using DCM of measured dispersion -347(5) ps/nm, spectrally filtered with a WDM to obtain 6 nm spectrum centered at 1563.7 nm, amplified via L-Band EDFA and temporally and polarization aligned to the other pump. The final pulse is measured on a sampling scope as shown in figure 4.14 right.

We perform an experiment using our weak coherent source, with an inherent line-width $<$ 100 kHz at 1283.5 nm. A pulse of about 4 ns is carved out of the CW signal and converted into a chirped broadband idler centered at 1278 nm. We estimate $|\alpha|^2 = 0.1$ ph/pulse. The conversion is shown in figure 4.14, as both signal and idler are separated temporally using a large DCM: from the depletion of the signal we measure a conversion efficiency of 40%, limited by the available power on the pulsed source.

After conversion, the idler is sent to a complementary DCM of dispersion $D = -279$ ps/nm at 1300 nm. Time of arrival enables us to distinguish signal from idler.

Since the temporal duration is below the resolution achievable with our APD detectors, we characterize the Field Correlation using an interferometric setup. The idler is filtered out using a WDM and injected into a fiber-based balanced Mach-Zender interferometer, with a free-space tunable delay and a piezo-mirror. We scan the interference fringe with the piezo-mirror, while slowly changing the

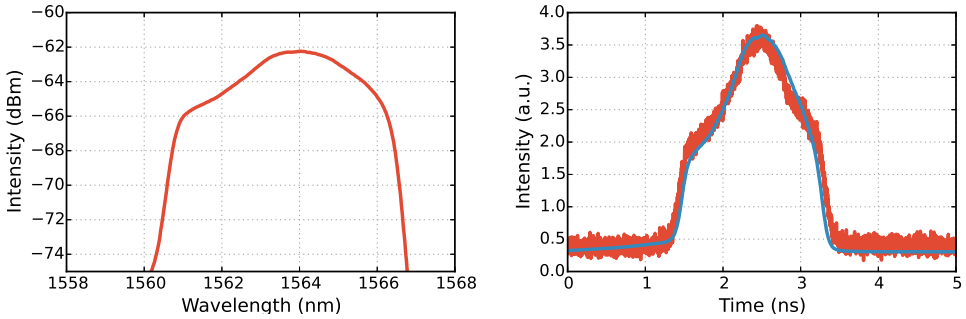

Figure 4.14: Chirped broadband pump characterization. Spectrum (left) as measured on OSA , and temporal profile (right), measured on fast detector.

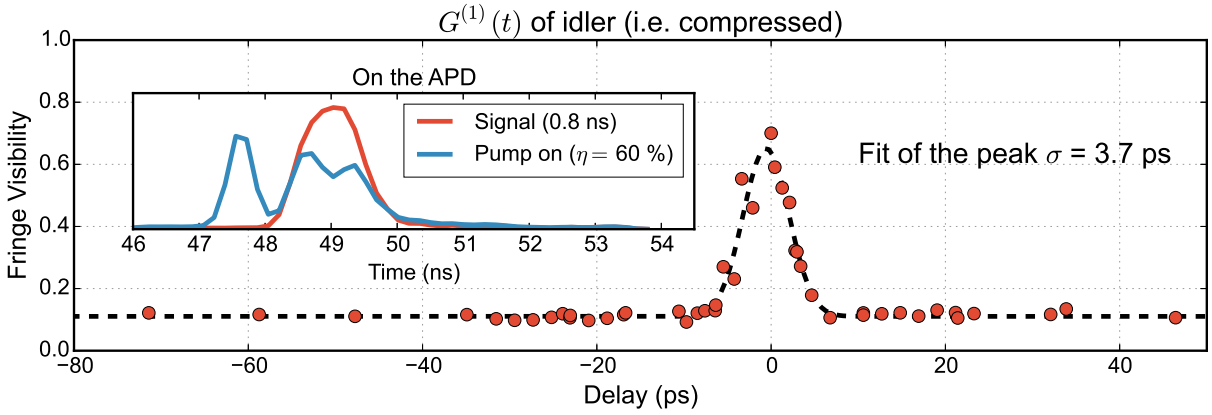

Figure 4.15: Temporal compression. Measurement of the first order autocorrelation.

delay. We detect the counts on the two APDs and record the time of arrival. The envelope of the visibility fringe is proportional to the field autocorrelation $g^{(1)}(\tau) = \langle\psi|E^{\dagger}(t+\tau)E(t)|\psi\rangle$ and to the Fourier transform of the field spectrum. The measurement in figure 4.15 shows a temporal autocorrelation of 3.6 ps, corresponding to a bandwidth of $\delta\lambda = 0.7$ nm for Gaussian pulses at 1280 nm and a compression factor of about x200.

4.4.2 Spectral compression

The reverse process of temporal compression is indeed spectral compression (or temporal magnification): a broadband signal is converted into a narrowband idler, and for, a transformed limited signal, temporal features are magnified by the same factor. Expressed in the time-lens paradigm, we are reversing the roles of dispersions, so that we are applying a linear chirp to a broadband signal to turn it into a narrowband idler.

The aim of this experiment is to reach large magnification for ultrashort waveforms (< 1 ps), so that they can be temporally characterized by single photon detectors (jitter 300ps for InGaAs, record of 100 ps for TSi superconductive nanowires [91]). Among the applications, the time-resolved characterization of broadband entangled photons, detection of ultrafast (> 20 GHz) time-bin entanglements, and optical time-domain reflectometry [92, 93].

Our experimental setup is very similar to temporal compression: we reverse the roles of dispersions on the signal, so that $\Phi_1 = -\Phi_p$. Large M are always attainable with large dispersions, with the drawback of large losses when implemented via dispersive fibers.

We employ single-mode fiber 1.3 km of SMF28 to disperse pump ($\Phi_1 = 4.6 \times 10^{-19}\,\mathrm{ns}^2$) and about 6 km of TrueWave fiber ($\Phi_p = -4.6 \times 10^{-19}\,\mathrm{ns}^2$). As output dispersion we use a DCM module $-1280\,\mathrm{ns/nm}$ with 9 dB of measured propagation losses.

In order to have a tunable broadband signal in 1280 nm range, we build a nonlinear fiberloop mirror that enables ultra-fast switching and modulation via XPM [94]. The source is depicted in figure 4.16: two 1300/1500 WDMs are placed in the interferometer path to couple in and out an amplified pump. The latter

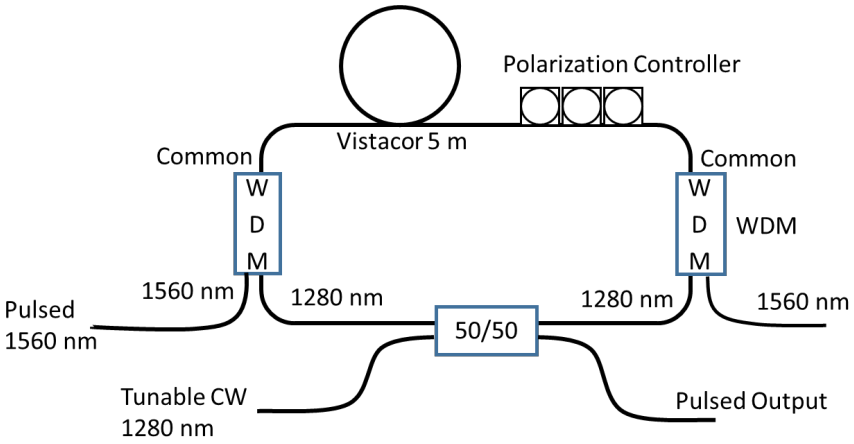

Figure 4.16: Nonlinear fiber-loop mirror

interacts with only the clockwise propagating field, hence applying a temporally localized phaseshift via XPM that is transformed into amplitude modulation at the output of the Sagnac loop. Polarization controllers are used to align the fields and to balance the interferometer. The pump is generated from the pulsed laser, ensuring temporal stability between signal and BS. The signal is seeded with the tunable 1300 laser. The temporal performance of such switch is limited by the group velocity mismatch $d_{ps} = \beta^{(1)}(\omega_p) - \beta^{(1)}(\omega_s)$. For SMF28, we estimate a walk-off time d_{ps} =2.6 ps/m. In order to generate shorter pulses, we utilize 4 m of the same Vistacor fiber we use for the BS interaction: in fact, the same dispersion profile that fulfills BS phasematching ensures small group velocity walk-off (d_{ps} =0.3 ps/m).

First we characterize conversion bandwidth: similarly to the previous case, we observe the conversion of a CW signal while scanning its wavelength, and we observe the conversion after the DCM. Results are shown on figure 4.17 A large range of frequencies (blue) centered at 1277.5 nm corresponds to a narrow idler centered at 1283.3 nm: this is the regime of spectral compression. For the signal at 1283.3 nm (red) the case is reversed: this is the regime of spectral broadening used

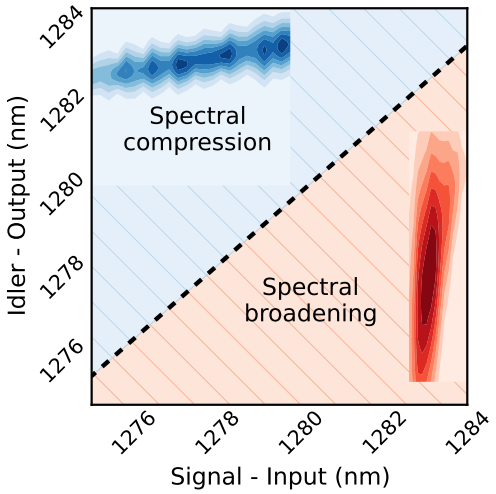

Figure 4.17: . Measurement of the bandwidth of the compression setup. As we scan a CW input signal, we observe the corresponding idler wavelength and bandwidth. For a large range of frequencies (blue) centered at 1277.5 nm corresponds a narrow idler centered at 1283.3 nm: this is the regime of spectral compression. For the signal at 1283.3 nm (red) the case is reversed: this is the regime of spectral broadening used for spectral compression.

for spectral compression. This measurement can be compared with theoretical curves of figure 4.13: this setup can compress signals with large bandwidth (5 nm, corresponding to $\delta\nu = 0.9$ THz)

Finally we inject the pulsed source, and observe the conversion. A tunable delay stage enables synchronization between BS gate and signal. Once the temporal overlap is obtained, we measure the idler after the DCM while scanning the delay, and report the results in figure 4.18. When synchronized, we measure a translation efficiency of η =75 %: this value is limited by the uneven pump spectrum.

The effect of the time-lens is to magnify the relative delay by the factor M = 27.6(4). This value differs from the expected M =36, probably because of dispersion mismatch introduced by the amplification of the pump, as well as from distortion of the BS phasematching condition introduced by$\beta^{(4)}$.

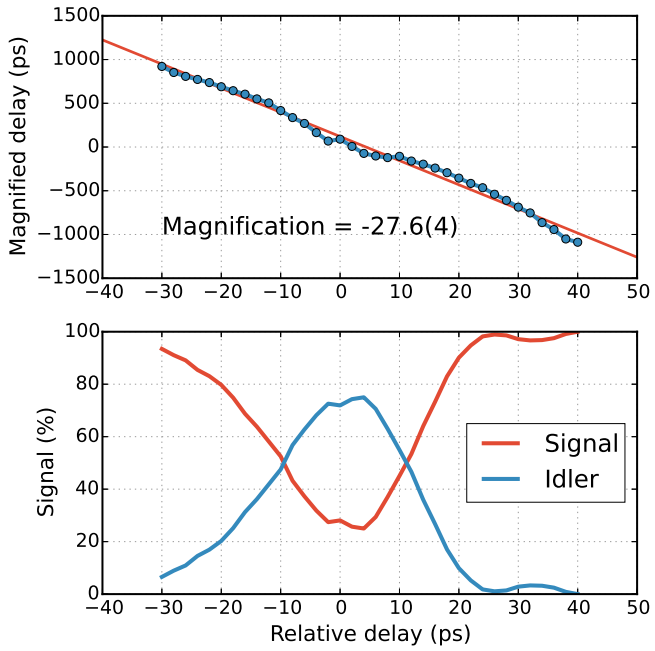

Figure 4.18: Temporal magnification: (top) delay of the signal vs. magnified delay of the idler. (bottom) Conversion efficiency: we observe a maximum efficiency $\eta =$ 75 % and temporal aperture of 30 ps FWHM

We finally create a delayed copy of the signal pulse using an unbalanced Mach-Zender interferometer. In figure 4.19 (left) we use an autocorrelator to measure the delay between the two pulse copies. For Δt =24.9 ns we observe a delay of 840 ps, for a magnification factor of about x30.

4.4.3 Single photon regime

Performing a time-lens experiment on an actual single photon proved to be difficult because of the limitations in our experimental system. For temporal compression, one would need a bright narrowband single photon source, such as quantum dots as in [68]. Another option would be cavity-enhanced spontaneous downconversion: we demonstrated bright generation of narrowband photons $\delta\nu < 1$ GHz in SiN

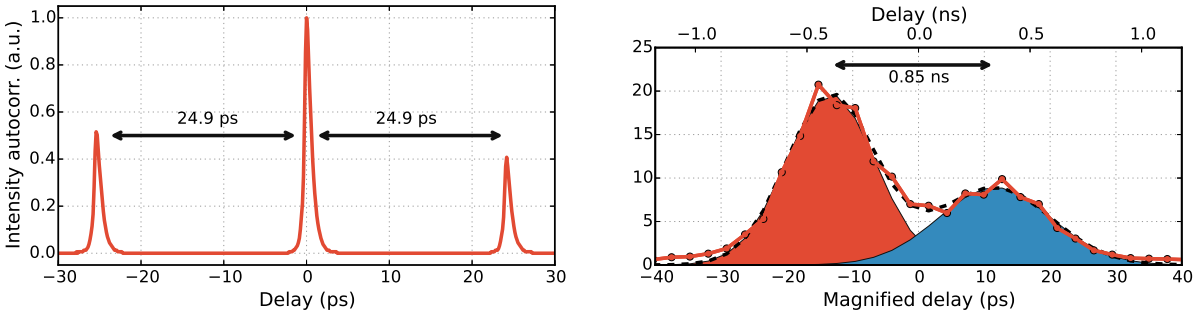

Figure 4.19: Resolving two pulses using temporal magnification. (left) Autocorrelator measurement of the relative delay of the two pulses.(right) Temporally resolving a delay of Δt =24.9 ps using detectors with jitter δt ≈400 ps.

microrings centered at 1550 nm and the same system could be utilized to generate photons in the 1280 nm band.

With regard to temporal magnification, broadband is easily obtainable for probabilistic sources: both heralded single photons and degenerate two photons can be generated from spontaneous downconversion. Unfortunately our setup cannot be synchronized to an external trigger, because of the passive nature of modelocking in the fiber laser used as pump: the low duty cycle of the current implementation of the system makes such experiment very hard and performance is effectively limited by the detectors' high dark counts. In order to observe temporal compression on single photon one can either utilize detector with better performance (such superconductive nanowire) or utilize the pump pulse to seed the single photon source and, in practice, achieving synchronization.

4.5 Conclusions

We demonstrate a BS setup capable of achieving high efficiency, low-loss and low-noise frequency translation. We utilized this setup as a test-bed for different ma-

nipulations of the temporal and spectral properties of single-photons and weak-coherent states: we proved a translation efficiency as high as 93 %, and identified the technical limitation that barred reaching perfect efficiency We proved that BS provides flexibility of configuration that leads to large acceptance bandwidth. In our time-lens experiments, we also reached very large internal efficiencies, up to 40 % for temporal compression and 75 % for spectral compression.

Our setup operates in a convenient regime for long distance communication, and can find direct applications in quantum cryptography and quantum key distribution [65].

CHAPTER 5

CHROMATIC QUBITS

For a long time the strange effects of quantum mechanics, such as the concept of superposition for macroscopic states [95], the irreversibility of the measurement act, and the nonlocal effects of entanglement [96], were considered to be open problem questioning the fondation of the theory. Starting in the 1980s, spurred by the first demonstration of violation of Bell's inequality as a distinctive feature that sets QM apart from a "classical" theory, several scientists started to wonder if these features of QM could lead to a different kind of logic. Famously Feynman proposed the use of QM to efficiently simulate QM [97]. Later on, Deutsch formalized the idea of a Quantum computer that could outperform classical computers on certain problems [98].

Compared to a classical computer register, where each bit can be either 0 or 1, a quantum bit (qubit) that can be a complex superposition of its states $|0\rangle$ and $|1\rangle$ is computationally more complex. Moreover when N qubits are described together, the resources needed to fully describe the system scale as 2^N complex numbers as opposed to N classical bits of a N-size register: simulating quantum systems becomes quickly computational expensive, so a quantum computer could efficiently simulate high-dimensional problems.

Evolution of quantum states is linear, so any transformation applied to a superposition applies independently to each component, appearing as processed in parallel. Unfortunately one can never observe the quantum waveform $|\psi\rangle$ directly, but only sample the probability distribution $|\psi|^2$. Hence, quantum efficient algorithms, e.g. Shore's prime number factorization or quantum oracles [99], make use of carefully designed interference patterns to answer to very specific problems that

are classically computationally expensive. It is still unproven whether this parallelism is purely quantum, though the applications in cryptography drove much of the interest in the earlier days of quantum information research.

Because of ease of implementation and very close relation between the classical and quantum evolution of the optical field, quantum optics has been a fertile field for many demonstrations of quantum computation [100]. Among the possible degrees of freedom in which to encode quantum information, polarization and path have been the most utilized, but they are limited in the number of dimensions achievable, i.e. the size of qubit (though advancements in integrated photonics enabled large scale path encoding). Time encoding can provide large multiplexing, but requires bulky optical delays and fast switches [101]. In the last few years, optical angular momentum has been explored as a promising way to access very large Hilbert space [102, 103].

Finally, frequency multiplexing has been investigated as a path to large-scale states: indeed, a parametric source can naturally provide a large level of spectral multiplexing and entanglement (i.e. from an OPO or a broadband single photon source) that has been explored as a resource for cluster states computation [104].

5.1 Ramsey Interferometer

Interferometry using discrete energy levels in nuclear, atomic or molecular systems is the foundation of a wide range of physical phenomena, enabling techniques such as nuclear magnetic resonance spectroscopy, electron spin resonance spectroscopy, Ramsey interferometry, laser and maser. It plays a unique role in quantum information processing as most qubits are implemented as energy superposition states of single quantum systems. The analogy between atomic/molecular optics and

nonlinear optics is well known [20]. Indeed, there are various cases where the complex dynamic of the light propagation in a nonlinear medium can be simplified to the coherent evolution of a two level system. For the first time, we bring this analogy a step further by applying it to quanta of light. Indeed, the photon is just like an atom level or a nuclear spin: it has a defined energy and if two energy levels are coupled together, quantum interference is possible. Here, we show how to experimentally generate energy superposition states of a single photon, to manipulate them with unitary transformations and to realize arbitrary projective measurements. To demonstrate the performance of this complete toolbox we implement high-visibility single-photon Ramsey interference.

5.1.1 Introduction

The model of a two level atom is arguably the simplest quantum system there is, yet its validity spans a wide variety of physical systems. Ramsey interferometry magnetic resonance imaging, and electron spin resonance spectroscopy, all rely on a 2-level system involving, respectively, actual molecular-atomic levels, nuclear spin, and electrononic spin; they also share the same kind of coupling between the levels leading to similar dynamics. Another common point is that the coupling between energy levels is achieved using (electro)magnetic fields. As (electro)magnetic fields can be tailored at will, this allows for many advanced techniques such as adiabatic elimination and stimulated Raman adiabatic passage in higher-dimensional atomic systems and spin locking in NMR. Quantum coherence has been particularly productive in improving time measurement: Ramsey interferometry on single Rydberg atoms has also allowed to measure nondestructively the number of photon in a cavity [105] while single spin manipulation using the same techniques

constitute one of the promising route towards quantum processing [106, 107, 108]. Translating those studies to photonics system implies controlling light with light which is essentially the definition of nonlinear optics.

Quantum interference involving systems in a superposition of different energies has been studied extensively over the past decades. Examples are numerous, and famous ones include nuclear magnetic resonance, where a collection of spins may evolve between a spin up and a spin down with different energies, and Ramsey interferometry, where an atom/molecule may be transferred from an excited level to the ground level. At the single quantum level, those techniques have also given rise to ground-breaking experiments testing foundations of quantum mechanics, such as decoherence [105, 109]. Matter-waves interferometer using energy levels of atoms has also been demonstrated [110] and used to measure gravity down to record breaking precision [32]. Those demonstrations clearly indicate that quantum interference involving systems in a superposition of different energies is a technique connected to the most fundamental basis of physics. Yet a very basic system has not been studied: a discrete two energy level system (i.e. frequency) for propagating photons. There are probably two reasons for that. The first is that photons are defined over a continuum of energies so that it may not be obvious at first what constitutes a two-level system for the energy of a photon. The second reason is that manipulating the frequency of a photon while preserving its coherence is not trivial. Here, we will show that it is sufficient to define any two arbitrary frequencies and manipulate them coherently via frequency translation to encode information on a two-energy-level of a single photon, which we will refer to as a "bichromatic qubit".

This new approach to encoding quantum information in the energy degree of

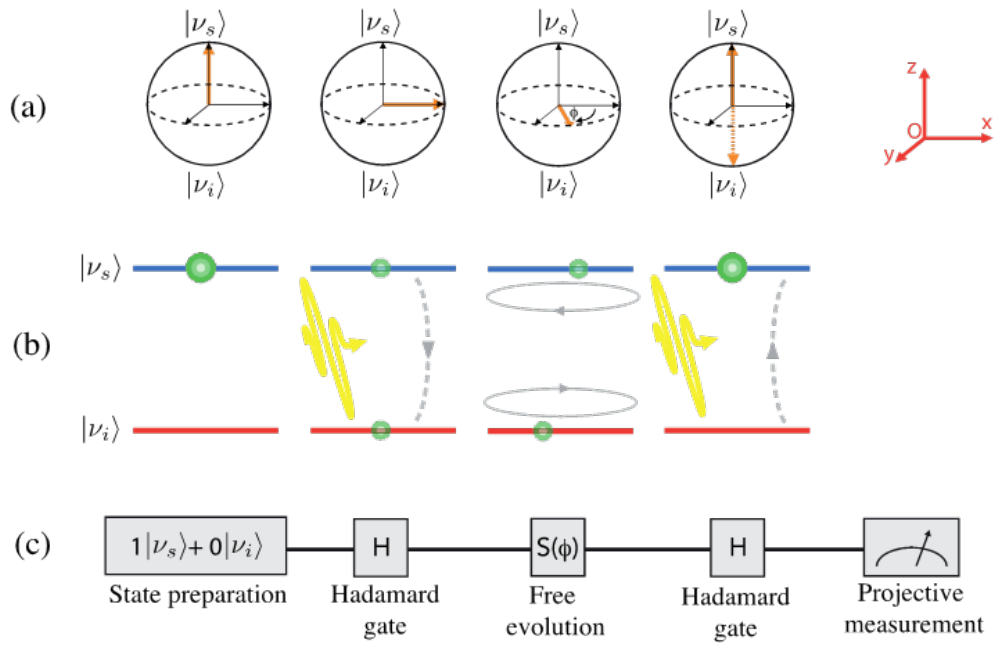

Figure 5.1: Principle of a Ramsey interference based on discrete energy levels of photons depicted as rotation on the Bloch sphere (a) evolution of a population on a two level system (b) or in term of quantum logic

freedom of single photons contrasts with many important works on frequency-encoded qubits: here it is trivial to define a qubit, whereas it was either practically impossible or complex in earlier works [111]. Indeed, it has been shown that photons from different frequencies interfere at the single quantum level [65] and that such two-party systems can violate Bell's inequalities [112]. However, those studies don't allow quantum logic operations in a two-dimensional Hilbert space such that a more complex definition of a frequency encoded qubit is required [112] to get closer to this ideal case. The core of our work is the frequency manipulation of single photons for which various successful studies using $\chi^{(2)}$ and $\chi^{(3)}$ nonlinear interactions [73, 74, 113, 20, 55, 53, 114] were demonstrated. It is also interesting to note that similar ideas are being developed for the purpose of sorting optical modes [70].

5.1.2 Principle and implementation

Figure 5.1 depicts the minimum set of functions required to perform quantum logic based on two energy levels of a single photon. This can be seen as a Ramsey interferometer and described either in terms of quantum logic operations, population evolution on a two level energy diagram, or rotations on a Bloch sphere where vectors pointing to the poles represent states in the two different energy levels. In a Ramsey interferometer, a two-level system undergoes two subsequent identical interactions with a resonating field of set intensity ($\pi/2$ pulse) separated by a long non-interacting interval of free evolution.

Here, the first step is to define two discrete energies a single photon can occupy and prepare it in one of them that we refer to as $|\nu_s\rangle$; that corresponds to being on a pole of the Bloch sphere. Then a $\pi/2$ pulse transforms the pure state into

a superposition of the form $1/\sqrt{2}(|\nu_s\rangle + |\nu_i\rangle)$; that corresponds to a $\pi/2$ rotation in the $O_{x,z}$ plane along the meridian of the Bloch sphere. The bichromatic qubit is subsequently left free to evolve for a time T. Free evolution means the system may acquire a relative phase $\varphi = 2\pi\delta\nu T$ because of the precession between the two levels of different energy. On the Bloch sphere, an azimuthal rotation occurs. Finally, a second $\pi/2$ pulse is applied that transforms the superposition state into a final state depending critically on the imparted phase φ. That is a second $\pi/2$ rotation in the $O_{x,z}$.

The projective measurement consist of detecting whether the photon has a frequency ν_s or ν_i and therefore reveals information on the phase φ. In order to practically prepare any state of a bichromatic qubit, i.e. implement the scheme depicted in figure 5.1, our toolbox needs 4 elements:

- (A) a bichromatic qubit defined by two-dimensional Hilbert space $\{|\nu_s\rangle, |\nu_i\rangle\}$,
- (B) a photon frequency converter capable of transferring the eigenvector back and forth ($\pi/2$ pulse),
- (C) control on the relative phase φ, and
- (D) a measurement of the energy of the final state.

The simplest way to create a bichromatic qubit (A) is simply to isolate a single photon at a given frequency $|\nu_s\rangle$ thus leaving the definition of its second energy level for later. There are many ways to generate such single photons but because the frequency converter (B) will impose some restrictions on the actual wavelength and bandwidth of the single photon we chose to use a frequency heralded photon source. Photon pairs are generated via spontaneous down conversion over frequencies ν_s and $\tilde{\nu}_h$ so that by spectrally filtering the broad flux of photons at the

frequency $\tilde{\nu}_h$ prior to its detection in a single photon detector, the partner photon is characterized both in the temporal domain via the timing resolution of the heralding detector and in the spectral domain via the correlation it has with its partner: $\nu_p = \nu_s + \tilde{\nu}_h$ where ν_p is the fixed frequency of a pump beam. Imparting a controllable relative phase between two optical frequencies (C) is trivial: it suffices to propagate the bichromatic photon over a length-tunable delays line. Measuring the final frequency (D) of the bichromatic photon is also trivial as it only requires to us to separate in two paths the two spectral component using any dispersive element. The single photon is detected using single photon detectors.

The remaining building block is thus the frequency converter (B) implemented with BS-FWM. From (2.5), BS-FWM acts as a rotation in the frequency Hilbert space $\{|\nu_s\rangle, |\nu_i\rangle\}$ and a $\pi/2$ rotation corresponds to $\gamma PL = \pi/8$ and that is a coherent evolution as $a_s(z = 0)$ and $a_s(z = 0)$ carry a phase as expected from a quantum coherent evolution. In addition, the evolution depicted by (2.5) also exhibits a phase dependence on the relative phase between the pump θ, so that care must be taken to keep the phase relationship between subsequent BS-FWM processes.

5.1.3 Experimental setup:

Our full experimental setup is depicted in figure 5.2. It shows our four building blocks (A-D) linked together to form a photonic Ramsey interferometer. Inset (A) shows the state preparation. A single photon at wavelength $\lambda_s = 1283.8$ nm is heralded by the detection, with a silicon avalanche photodiode (Si-APD); its partner photon is generated at $\lambda_h = 940$ nm by type-0 spontaneous downconversion from a PPLN crystal pumped by a CW laser emitting at 543 nm. The heralding

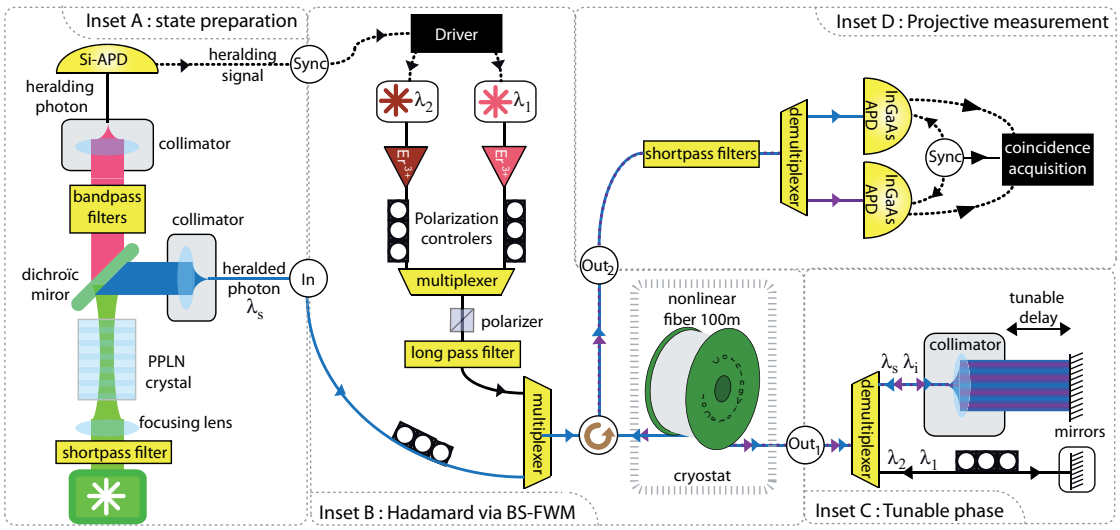

Figure 5.2: Experimental implementation of Ramsey interferometry with photons.

photon is spectrally filtered to select a signal photon at 1283 nm with a narrow bandwidth of 0.5 nm. The heralded photon is separated out of the residual pump, and then coupled into an optical fiber to be routed to the second part of the setup. Alternatively, we used a tunable laser to align, synchronize and characterize the setup. A tunable attenuator was used to reach the weak coherent state of less than 0.1 photon per gate. Signal wavelength and bandwidth are selected to accommodate the frequency converter (inset B).

The design of the frequency converter was discussed in chapter 4 and is depicted in inset (B) of figure 5.2. In our setup, we employ a fiber-based BS-FWM scheme to couple two frequencies within the same optical band (O-band), using only standard telecommunication components. The nonlinear medium is a dispersion shifted fiber (DSF) of measured zero GVD wavelength $\lambda_0 = 1413$ nm. Pump pulses are generated on demand by current modulation of laser diodes emitting at $\lambda_1 = 1551.7$ nm and $\lambda_2 = 1558.1$ nm. The nanosecond pulses are amplified to multi-Watt level via cascaded erbium-doped fiber amplifiers, synchronized and superposed with the signal photon in the DSF using WDM add- and-drop filters. The polarization of

all three fields is aligned to be parallel.

To apply a controllable phase, we simply separated the pump beams from the bichromatic photon and set a tunable free space delay on its path (inset (C)). Indeed, we expressed by equation (2.5) that the BS-FWM process depends on the relative phase between the two spectral components of the single photon, but it also depends on the relative phase of the two pump photons. As we want to preserve the phase relationship between pumps and signal for driving any subsequent BS-FWM interaction, we must control (or fix) independently the pump relative phase from the bichromatic qubit one; especially, the precession acquired by the two pumps (as in $\phi_{p1} - \phi_{p2}$ in eq. (2.5)) would exactly cancel out with the bichromatic qubit phase, the two being of equal value in free space (not in a dispersive media). In this case, the phase $\varphi = 2\pi\Delta x(\nu_s - \nu_i)/c$ is applied over the bichromatic photon for propagation over a distance Δx. The inset (D) of figure 5.2 shows how the projective measurements are performed. First, remaining photons from the optical pump in frequency converters are suppressed using short pass filters. Then the two spectral components of the bichromatic qubit are separated using commercially available wavelength division demultiplexers and single photon detection on both arms is operated using InGaAs avalanche photodiodes.

5.1.4 Ramsey interference

The toolbox we have introduced allows us, in principle, to generate any state of a bichromatic qubit and thus set a state anywhere on the Bloch sphere. To verify this statement, we perform a Ramsey interference experiment. The setup is depicted again in figure 3 and consist of the four building blocks we have introduced. First the state is prepared at frequency νs (A), then a $\pi/2$ pulse is applied using the

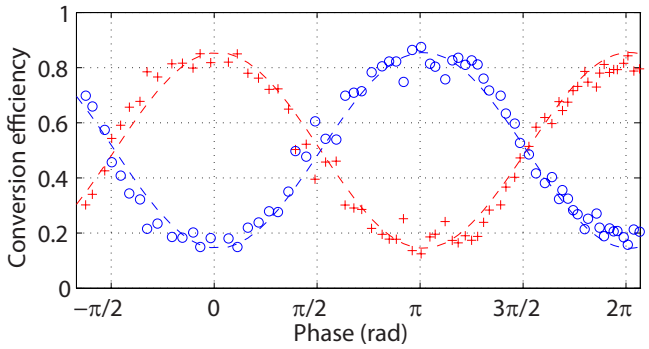

Figure 5.3: (a) classical (b) quantum

frequency converter (B), then a tunable phase is imparted on the bichromatic qubit (C), then again a $\pi/2$ pulse is applied using the same frequency converter (B) but in the reverse direction and, finally, the final state is reconstructed via frequency demultiplexing and single photon detection (D). As compared with their individual use, the elements (A-D) require a few specific adjustments. First, the BS-FWM pump power P is adjusted to give a conversion efficiency of 1/2 so that the bichromatic qubit exits (B) as a balanced superposition of the two frequencies ν_s and ν_i. Then in the tunable phase delay stage (C), the pump and signal arms are kept to nearly equal length so that the pulses still overlap on the reflected single photon (pulse duration is much larger than the fringe size, and polarization is kept parallel using a polarization controller) before they propagate back in the DSF.

The result of the Ramsey interference is depicted in fig. 5.3 and shows the signal conversion to the idler frequency as a function of the imparted phase. As expected, the interference pattern shows fringes corresponding to the probability $P(\nu_s) = \sin(\varphi/2)^2$ and $P(\nu_i) = \cos(\varphi/2)^2$. The interference pattern shows fringes over a π phase that correspond to free space propagation of 0.36 mm. The presence of interference fringes is proof that the underlining BS-FWM process preserves

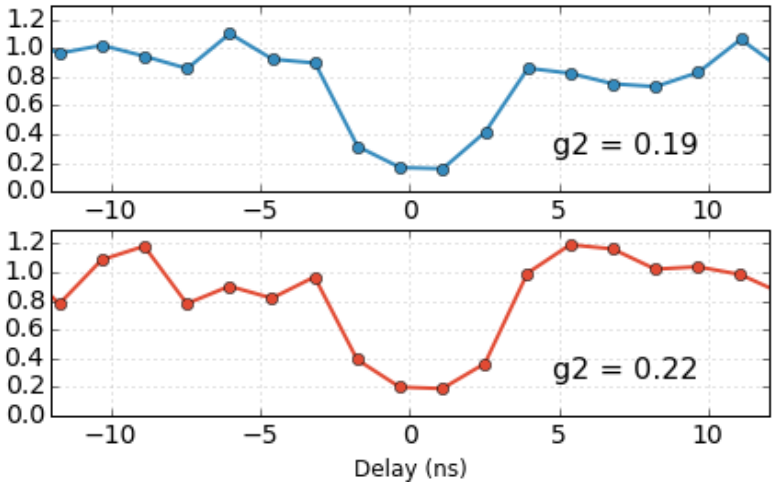

Figure 5.4: $g^{(2)}(\tau)$ for pumps off and on.

the coherence of the quantum fields. The visibility of those fringes is nearly 50 %, limited by two factors: the bandwidth of the single photon is very close to the acceptance bandwidth of the BS-FWM which limits the maximum conversion to 80% (see chapter 4); in addition, the pump experience some loss (2.8 dBm) in the tunable delay which result in the second rotation being less than $\pi/2$ as targeted. The measurement has also been carried out for a coherent state and shows indeed better visibility exceeding 80% because of its intrinsically smaller bandwidth. We also verify that the process is suitable for quantum application and preserves Fock states (i.e. technical noise is not relevant), so we measure the second order correlation function $g^{(2)}(\tau = 0)$ of the single photon. This is done by replacing the demultiplexer with a balanced beam splitter in the projective measurement (D). We see that whether we apply a transformation on the Bloch sphere or not (pump beams turned off), the $g^{(2)}(\tau = 0)$ function stays at a value of 0.2 (figure 5.4)

5.2 High-dimensional frequency multiplexing

In this final section, we computationally explore the interaction of a large set of frequency channels via BS, driven by several pumps, as a way to achieve dense quantum frequency multiplexing, as well as to explore novel BS regimes.

Let's define $\omega_p^{(i)}$ a comb of N pump frequencies separated by $\Delta\omega$ driving a BS interaction for M $\omega_s^{(i)}$ frequency bins[1]. Each pair $\omega_p^{(l)}, \omega_p^{(m)}$ in principle drives interaction between every two signal bins $\omega_s^{(i)}, \omega_s^{(j)}$ with energy difference $(l - m)\Delta\omega = (i - j)\Delta\omega$, modulated by the phasematching condition $exp(i\kappa_{i,j,l,m}z)$. For example, two pumps in adjacent bins drives all the nearest neighbors signal pair as in a cascaded process.

For the general case, the evolution of the signal field at $\omega_s^{(i)}$ is

$$\frac{d}{dz}A_i(z) = i2\gamma \sum_{l-m=i-j} \sqrt{P_l P_m} e^{i\left(\phi_p^{(l)} - \phi_p^{(m)}\right)} e^{+i\kappa_{i,j,l,m}z} A_j(z) \tag{5.1}$$

The final system of equations is a realization of the well known problem of coupled oscillators [115]. One particular optical realization, in the form of optical latticeof coupled waveguides [116] enabled the simulation of large systems, exhibiting phenomena such as Anderson localization and random diffusion.

Frequency multiplexing coupled via BS is different from other implementations in two aspects: the first is the selection rule $l - m = i - j$, which can lead to non-trivial interaction geometries (most implementations are limited to near neighbor coupling); the second is the phasematching term.

[1] In this section, we assume monochromatic fields. Similar results can be obtained for pulses.

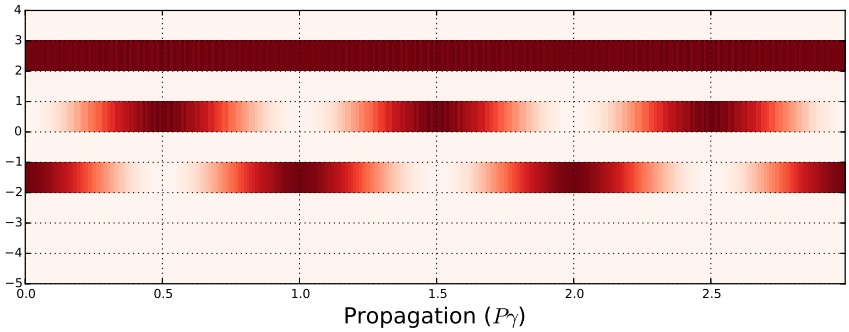

Figure 5.5: Coupled frequency bins for 2 pumps at $l, m = -1, 1$ and for $\delta\omega_{bs} \ll \Delta\omega$: a signal injected at oscillation only between the $i, j = (-1, 1)$.

In order to understand better how the system behaves under different conditions, let's assume that each comb is centered at the optimal phasematching $\bar{\omega}_p = \omega_{ZDW} + \Delta\Omega_p$, $\bar{\omega}_s = \bar{\omega}_{DZW} - \Delta\Omega + \Delta\epsilon$, so that each line is parametrized as $\omega_{p,s}^{(i)} = \bar{\omega}_{p,s} + \frac{i}{2}\Delta\omega$. Let's also assume the regime $2\Delta\omega/\Delta\Omega \ll 1$, so that we can consider both $\Delta\epsilon$ and the acceptance bandwidth $\delta\omega_{bs}$ not dependent on i.

All the following results are obtained by numerical integration of equation (5.1). Propagation is in natural units of $\pi/2\gamma P$

The simplest case is for $N = 2$ pumps sitting at $l = -1, 1$: for $\delta\omega_{bs} \ll \Delta\omega$ oscillation only between the $i, j = (-1, 1)$ pair is permitted, and we recover the dynamics discussed already in this work. In figure 5.5 we inject a field at different channels and observe that oscillations appear only between $i, j = (-1, 1)$. We can have further evidence of the selectivity if we now consider the two pumps sitting at any frequency pairs: phasematching is still such that only two signal fields will be interacting. By increasing N we can determine coupling between several modes at once, as we show in figure 5.6: in the top figure, for N =3 we observe how the injected signal breaths over three modes (with periodicity 2/3); in the bottom figure, four modes are coupled with pumps of different powers, determining a

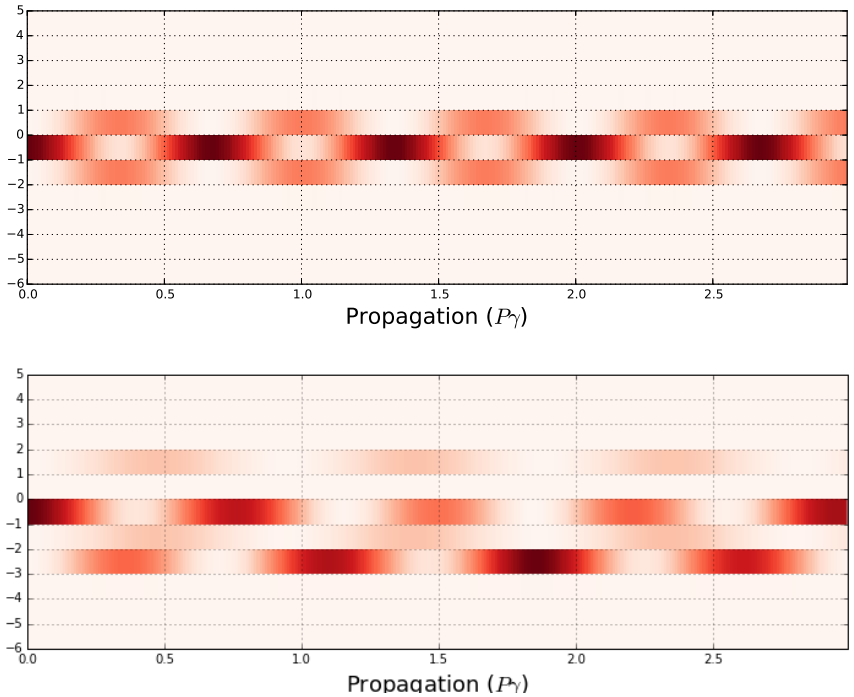

Figure 5.6: Coupled frequency bins for N $>$ 2 pumps $\delta\omega_{bs} \ll \Delta\omega$. (top) pumps at $l = -1, 0, 1$ (bottom) $l = -2, 0, 1, 2$, and pump powers respectively $P = 0.5, 1, 0.5, 1$

complicated pattern of interference.

For $\delta\omega_{bs} > \Delta\omega$ we obtained the cascaded process with higher orders up to $i \simeq \delta\omega_{bs}/\Delta\omega$. This system evolves similarly to an array of coupled waveguides, where phasematching sets reflective boundary conditions. If we excite a single mode in the center of the array (figure 5.7), we observe progressive excitation of multiple orders until the boundaries are reached: at that point the excitation is reflected and generates interference patterns.

5.3 Conclusion

Here we have introduced the building blocks for coding quantum information on a frequency qubit. We have shown that we can perform any rotation on the corresponding Bloch sphere using a Ramsey interference experiment. Indeed, in quantum information such a bichromatic qubit can serve as a stable carrier over long distances, but also as a link between two quantum systems operating at different frequencies. This is very relevant for quantum key distribution [117, 118, 119, 120] whose future expansion to longer distances will probably depends on quantum relays operating at very specific frequencies. Encoding quantum information on the frequency degree of freedom of single photon may also provide a practical advantage as the interferometer we present does not require phase stability down to the wavelength range as fringes depends on the larger beating wavelength $\Delta\lambda = c/\delta\nu$.

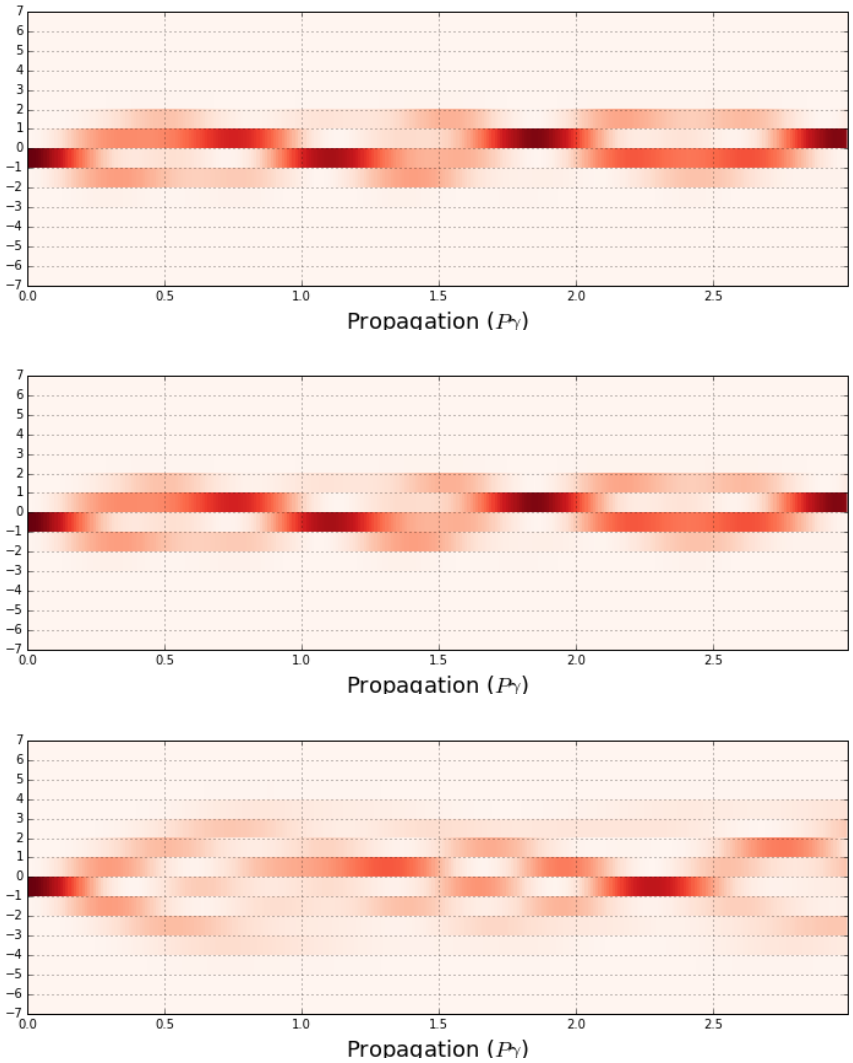

Figure 5.7: Coupled frequency bins for 2 pumps at $l, m = -1, 1$, for increasing values of $\delta\omega_{bs} \gg \Delta\omega$: a signal injected at the center frequency undergoes diffusion.

CHAPTER 6

CONCLUSIONS AND FUTURE WORKS

In the context of classical optics, frequency translation is an alternative tool for signal processing and waveform manipulation. It has enabled us to prove a novel approach to cloaking experiments, extending the time-space paradigm to new class of time reversible phenomena. In the context of quantum optics, we demonstrated a very low-noise and high-efficiency setup that preserves quantum properties. Stepping forward from the demonstration of high-efficiency conversion, we utilized the process for novel manipulation of the quantum waveform at the single photon level. Using the time-lens paradigm, we demonstrated spectral-broadening and spectra-compression, reaching very large conversion factors together with high-efficiency, which is hardly achievable with other methods. Finally, we showed how information can be encoded into and read from a frequency superposition, and how BS can be used to control large sets of frequency bins, paving the way to high-dimensional frequency multiplexed qubits.

Frequency translation was initially developed as a means to interface different elements of a large scale quantum architecture: in the two decades from the first demonstration this tool has mostly been perfected for just this single goal: a perfect and noiseless conversion of frequency. In this work, we indeed achieved such goal using BS, but we also showed that BS is a tool for a larger set of operations: on one hand, the reversibility of the process naturally matches with concept of time-space duality, and high-efficiency BS can be used impart large, arbitrary phase-modulations for complex manipulation of signals. On the other hand, the coherence of the process enables us to drive the interaction between different frequencies.

As demonstrated in this work, once a reliable setup is available, a plethora of different configurations and manipulations can be performed: here we presented only few examples, but we believe more application can be found. In addition to a further exploration of the performance of the setup with single photon states, here we provide few additional directions.

6.1 Translation for large frequency detuning

BS conversion presents the flexibility to operate between widely different regimes. In fact, all the equations presented, including phasematching, work if we place one of the pumps very close to the signal, reversing the role of ω_{p1} and ω_i: in this configuration, BS enables translation over a large frequency span.

This regime has important applications: first of all, the ability, already sought by $\chi^{(2)}$-based converter, to connect telecomm infrared photons to solid based quantum devices operating in the near-infrared and visible, as was recently demonstrated on SiN microrings for a conversion across 700 nm [17]. Again, BS-based conversion has the advantage of providing the flexibility of tuning the target frequencies by just modifying the pumps wavelengths, while $\chi^{(2)}$ systems relay on a combination of pump and dispersion tuning. Moreover, the presence of strong $\chi^{(3)}$ nonlinearity on many photonic platforms leads the way to monolithic integration of source and converter.

One line of research would be to extend the range of conversion even farther: to one end of the spectrum, the very near infrared, enabling a larger class of quantum system to be interfaced (such as atomic vacancies and quantum dots), and to the other end of the spectrum the mid- and far-infrared, for enhanced detection in spectroscopy and astrophysics applications.

6.2 Frequency-multiplexed quantum source

Single photon sources can be divided into two broad categories: *single emitter* sources, such as a trapped ion, an atom or a correlated ensemble, where the excitation of the system corresponds to the emission of exactly one photon, and *heralded* sources, parametric downconversions where one excitation generates several photons, but a partial measurement of the system (e.g. the detection of an heralded photon) selects the cases where only one photon is generated.

Because the latter depend on stochastic events, they are often referred as *probabilistic* sources, and the internal probability cannot reach 100 % of photon emission per excitation (e.g. for downconverted source, $P = 5$ %). On the other hand, the former category can provide on-demand photons, on the other hand, they are difficult to implement for an integrated system, often requiring cryogenic cooling and magnetic traps.

One can improve the brightness of a source by multiplexing several sources and post-selecting only the ones for which the heralding event clicks. In fact, the probability of at least one source clicking grows quickly with the number of sources [121]. Several demonstrations utilize different degrees of freedom, such as polarization [122], time [123, 124], paths [125] or a combination of these. The major limiting factor for integrated multiplexed sources has been losses due to routing: while low losses 2x2 switches are possible (i.e. using an interferometric switch), they scale for increasing numbers of inputs/outputs, limiting in practice the advantage of multiple sources [**?**].

We propose to utilize frequency as a degree of freedom and heralded BS to deterministically route single photons into a frequency mode. Spontaneous down-

conversion sources can be filtered into a broad comb of frequency channels matching a BS system. As we demonstrated, BS can selectively convert a broadband into a single mode by just tuning one of the pump frequency. More importantly, losses experienced by the system do not scale with the number of frequency channels.

6.3 Bosonic sampling with frequency bins

Recent advancements in device fabrication have enabled the realization of large monolithic interferometric setups (or optical lattices), in the form of cascaded Mach-Zender interferometers [126] or waveguide arrays. These new devices partially overcome the overhead introduced by maintaining a large free-space setup to interferometric stability.

On such systems one can study the evolution of arbitrary optical states over a large dimensionality. The simplest of the problems, that is, quantum random walk, already distinguishes itself from the classical analogue, and becomes substantially different when two or more photons are injected at the same time [127]. Some classical computational problems can be reformulated in this context, but they don't offer an effective improvement in performance [128]. Nonetheless, it was noticed only recently [129] that calculating the state generated by N single photons injected from multiple ports of a large interferometric system, i.e. a set of beamsplitters and delays, is computationally hard and practically not feasible for $N > 50$.

The *bosonic sampling* problem has quickly become a paradigm problem in the quantum optics community, as a gateway to experimentally demonstrate a truly quantum computational speedup. In fact, some of the requirements that normally

limit large scale implementation of a system, for example, large single photon nonlinearities in optical implementations, do not apply in this context. Though the photons do not interact through their propagation, the symmetries deriving from their bosonic nature creates entanglement in the occupational number statistics, of which Ou-Ho-Mandel interference is simplest case.

Extending the results of chapter 5, frequency multiplexing provides access to a large-dimensional space that can be tailored just by manipulation of pump power and relative phase: multiple single photons can be generated by a cavity enhanced downconversion source and let propagate through optical lattices defined by a shaped comb of pumps, to be then separated via low-loss WDM.

BIBLIOGRAPHY

[1] J. A. Armstrong, N. Bloembergen, J. Ducuing, and P. S. Pershan, "Interactions between Light Waves in a Nonlinear Dielectric," *Phys. Rev.*, vol. 127, pp. 1918–1939, Sept. 1962.

[2] P. Franken, A. Hill, C. Peters, and G. Weinreich, "Generation of Optical Harmonics," *Phys. Rev. Lett.*, vol. 7, pp. 118–119, Aug. 1961.

[3] R. R. Alfano and S. L. Shapiro, "Observation of Self-Phase Modulation and Small-Scale Filaments in Crystals and Glasses," *Phys. Rev. Lett.*, vol. 24, pp. 592–594, Mar. 1970.

[4] M. M. Fejer, "Nonlinear Optical Frequency Conversion: Material Requirements, Engineered Materials, and Quasi-Phasematching," in *Beam Shap. Control with Nonlinear Opt. SE - 13* (F. Kajzar and R. Reinisch, eds.), vol. 369 of *NATO Science Series: B:*, pp. 375–406, Springer US, 1998.

[5] J. E. Midwinter, "Image conversion from 1.6 μm to the visible in lithium niobate," *Appl. Phys. Lett.*, vol. 12, p. 68, Oct. 1968.

[6] K. F. Hulme and J. Warner, "Theory of Thermal Imaging Using Infrared to Visible Image Up-Conversion," *Appl. Opt.*, vol. 11, p. 2956, Dec. 1972.

[7] Z. Li and G. Li, "Ultrahigh-speed reconfigurable logic gates based on four-wave mixing in a semiconductor optical amplifier," *IEEE Photonics Technol. Lett.*, vol. 18, pp. 1341–1343, June 2006.

[8] R. Salem, M. A. Foster, and A. L. Gaeta, "Application of space-time duality to ultrahigh-speed optical signal processing," *Adv. Opt. Photonics*, vol. 5, p. 274, Aug. 2013.

[9] K. Uesaka, K.-Y. Wong, M. Marhic, and L. Kazovsky, "Wavelength exchange in a highly nonlinear dispersion-shifted fiber: theory and experiments," *IEEE J. Sel. Top. Quantum Electron.*, vol. 8, pp. 560–568, May 2002.

[10] P. Kumar, "Quantum frequency conversion," *Opt. Lett.*, vol. 15, p. 1476, Dec. 1990.

[11] K. Inoue, "Tunable and selective wavelength conversion using fiber four-wave mixing with two pump lights," *IEEE Photonics Technol. Lett.*, vol. 6, pp. 1451–1453, Dec. 1994.

[12] M. E. Marhic, Y. Park, F. S. Yang, and L. G. Kazovsky, "Widely tunable spectrum translation and wavelength exchange by four-wave mixing in optical fibers," *Opt. Lett.*, vol. 21, pp. 1906–1908, Dec. 1996.

[13] R. W. Boyd, *Nonlinear optics*, vol. 5 of *Electronics & Electrical*. Academic Press, 2003.

[14] J. Jackson, *Classical Electrodynamics*. Wiley, 1998.

[15] C. Pollock and M. Lipson, *Integrated Photonics*. Springer, 2004.

[16] R. Provo, S. Murdoch, J. D. Harvey, and D. Méchin, "Bragg scattering in a positive beta4 fiber," *Opt. Lett.*, vol. 35, pp. 3730–3732, Nov. 2010.

[17] Q. Li, M. I. Davanco, and K. Srinivasan, "Chip-based frequency conversion by four-wave-mixing Bragg scattering in Si_3N_4 microrings," in *CLEO 2015*, (Washington, D.C.), p. JTu5A.43, OSA, May 2015.

[18] Y. Q. Xu, M. Erkintalo, G. Genty, and S. G. Murdoch, "Cascaded Bragg scattering in fiber optics.," *Opt. Lett.*, vol. 38, pp. 142–4, Jan. 2013.

[19] C. Cohen-Tannoudji, B. Diu, F. Laloe, and B. Dui, *Quantum Mechanics (2 vol. set)*. Wiley-Interscience, Oct. 2006.

[20] A. P. VanDevender and P. G. Kwiat, "Quantum transduction via frequency upconversion (Invited)," *J. Opt. Soc. Am. B*, vol. 24, pp. 295–299, Feb. 2007.

[21] H. J. McGuinness, M. G. Raymer, and C. J. McKinstrie, "Theory of quantum frequency translation of light in optical fiber: application to interference of two photons of different color.," *Opt. Express*, vol. 19, pp. 17876–907, Sept. 2011.

[22] A. Ekert, "Entangled quantum systems and the Schmidt decomposition," *Am. J. Phys.*, vol. 63, p. 415, May 1995.

[23] U. Leonhardt, "Optical conformal mapping," *Science (80-.).*, vol. 312, pp. 1777–1780, 2006.

[24] J. B. Pendry, D. Schurig, and D. R. Smith, "Controlling electromagnetic fields," *Science (80-.).*, vol. 312, pp. 1780–1782, 2006.

[25] U. Leonhardt and T. Tyc, "Broadband invisibility by non-Euclidean cloaking," *Science (80-.).*, vol. 323, pp. 110–112, 2009.

[26] U. K. Chettiar, A. V. Kildishev, V. Shalaev, and W. Cai, "Optical cloaking with metamaterials," *Nature*, vol. 1, pp. 224–227, 2007.

[27] S. A. Cummer, "Scattering theory derivation of a 3d acoustic cloaking shell," *Phys. Rev. Lett.*, vol. 100, p. 24301, 2008.

[28] Y. Lai, H. Chen, Z. Q. Zhang, and C. T. Chan, "Complementary media invisibility cloak that cloaks objects at a distance outside the cloaking shell," *Phys. Rev. Lett.*, vol. 102, p. 93901, 2009.

[29] L. H. Gabrielli, J. Cardenas, C. B. Poitras, and M. Lipson, "Silicon nanostructure cloak operating at optical frequencies," *Nat. Photon.*, vol. 3, pp. 461–463, 2009.

[30] J. Li Valentine, L. Zentgraf, T. G. Bartal, and X. Zhang, "An optical cloak made of dielectrics," *Nat. Mater.*, vol. 8, pp. 568–571, 2009.

[31] J. Li and J. B. Pendry, "Hiding under the carpet: a new strategy for cloaking," *Phys. Rev. Lett.*, vol. 101, p. 203901, 2008.

[32] D. A. B. Miller, "On perfect cloaking," *Opt. Express*, vol. 14, pp. 12457–12466, 2006.

[33] R. A. Weder, "A rigorous analysis of high-order electromagnetic invisibility cloaks," *J. Phys. A*, vol. 41, p. 65207, 2008.

[34] A. Greenleaf, "Lassas, M. & Uhlmann, G. Anisotropic conductivities that cannot be detected by EIT. Physiol. Meas.," 2003.

[35] D. Schurig, "Metamaterial electromagnetic cloak at microwave frequencies," *Science (80-.).*, vol. 314, pp. 977–980, 2006.

[36] H. Chen, B. I. Wu, B. Zhang, and J. A. Kong, "Electromagnetic wave interactions with a metamaterial cloak," *Phys. Rev. Lett.*, vol. 99, p. 63903, 2007.

[37] M. Fridman, A. Farsi, Y. Okawachi, and A. L. Gaeta, "Demonstration of temporal cloaking.," *Nature*, vol. 481, pp. 62–5, Jan. 2012.

[38] M. W. McCall, A. Favaro, P. Kinsler, and A. Boardman, "A spacetime cloak, or a history editor," *J. Opt.*, vol. 13, p. 24003, 2011.

[39] B. H. Kolner, "Space-time duality and the theory of temporal imaging," *IEEE J. Quantum Electron.*, vol. 30, pp. 1951–1963, 1994.

[40] B. H. Kolner and M. Nazarathy, "Temporal imaging with a time lens.," *Opt. Lett.*, vol. 14, no. 12, pp. 630–632, 1989.

[41] C. V. Bennett and B. H. Kolner, "Principles of parametric temporal imaging. I. System configurations," *Quantum Electron. IEEE J.*, vol. 36, no. 4, pp. 430–437, 2000.

[42] C. V. Bennett and B. H. Kolner, "Principles of parametric temporal imaging. II. System performance," *IEEE J. Quantum Electron.*, vol. 36, pp. 649–655, June 2000.

[43] R. Salem, "Optical time lens based on four-wave mixing on a silicon chip," *Opt. Lett.*, vol. 33, pp. 1047–1049, 2008.

[44] M. A. Foster, "Ultrafast waveform compression using a time-domain telescope," *Nat. Photon.*, vol. 3, pp. 581–585, 2009.

[45] G. P. Agrawal, "Nonlinear Fiber Optics," 2007.

[46] J. M. Lukens, D. E. Leaird, and A. M. Weiner, "A temporal cloak at telecommunication data rate," *Nature*, vol. 498, pp. 205–208, June 2013.

[47] J. M. Lukens, A. J. Metcalf, D. E. Leaird, and A. M. Weiner, "Temporal cloaking for data suppression and retrieval," *Optica*, vol. 1, p. 372, Nov. 2014.

[48] P. Y. Bony, M. Guasoni, P. Morin, D. Sugny, A. Picozzi, H. R. Jauslin, S. Pitois, and J. Fatome, "Temporal spying and concealing process in fibre-optic data transmission systems through polarization bypass.," *Nat. Commun.*, vol. 5, p. 4678, Jan. 2014.

[49] J. H. Shapiro, "Architectures for long-distance quantum teleportation," *New J. Phys.*, vol. 4, pp. 47–47, July 2002.

[50] H. J. Kimble, "The quantum internet.," *Nature*, vol. 453, pp. 1023–30, June 2008.

[51] J. Huang and P. Kumar, "Observation of quantum frequency conversion," *Phys. Rev. Lett.*, vol. 68, pp. 2153–2156, Apr. 1992.

[52] M. A. Albota and F. N. C. Wong, "Efficient single-photon counting at 1.55 microm by means of frequency upconversion.," *Opt. Lett.*, vol. 29, pp. 1449–1451, July 2004.

[53] C. Langrock, E. Diamanti, R. V. Roussev, Y. Yamamoto, M. M. Fejer, and H. Takesue, "Highly efficient single-photon detection at communication wavelengths by use of upconversion in reverse-proton-exchanged periodically poled LiNbO3 waveguides," *Opt. Lett.*, vol. 30, p. 1725, July 2005.

[54] A. P. Vandevender and P. G. Kwiat, "High efficiency single photon detection via frequency up-conversion," *J. Mod. Opt.*, vol. 51, pp. 1433–1445, July 2004.

[55] S. Zaske, A. Lenhard, and C. Becher, "Efficient frequency downconversion at the single photon level from the red spectral range to the telecommunications C-band.," *Opt. Express*, vol. 19, pp. 12825–36, June 2011.

[56] S. Tanzilli, W. Tittel, M. Halder, O. Alibart, P. Baldi, N. Gisin, and H. Zbinden, "A photonic quantum information interface.," *Nature*, vol. 437, pp. 116–20, Sept. 2005.

[57] S. Ramelow, A. Fedrizzi, A. Poppe, N. K. Langford, and A. Zeilinger, "Polarization-entanglement-conserving frequency conversion of photons," *Phys. Rev. A*, vol. 85, p. 013845, Jan. 2012.

[58] S. Ates, I. Agha, A. Gulinatti, I. Rech, M. T. Rakher, A. Badolato, and K. Srinivasan, "Two-photon interference using background-free quantum frequency conversion of single photons emitted by an InAs quantum dot," *Phys. Rev. Lett.*, vol. 109, p. 147405, Oct. 2012.

[59] C. J. McKinstrie, J. D. Harvey, S. Radic, and M. G. Raymer, "Translation of quantum states by four-wave mixing in fibers," *Opt. Express*, vol. 13, no. 22, p. 9131, 2005.

[60] A. H. Gnauck, R. M. Jopson, C. J. McKinstrie, J. C. Centanni, and S. Radic, "Demonstration of low-noise frequency conversion by bragg scattering in a fiber.," *Opt. Express*, vol. 14, pp. 8989–94, Oct. 2006.

[61] M. Bradford, K. C. Obi, and J.-T. Shen, "Efficient single-photon fre-

quency conversion using a sagnac interferometer," *Phys. Rev. Lett.*, vol. 108, p. 103902, Mar. 2012.

[62] N. Matsuda, "Single-photon frequency conversion using cross-phase modulation," in *CLEO 2014*, (Washington, D.C.), p. FW1A.6, OSA, June 2014.

[63] J. T. Hill, A. H. Safavi-Naeini, J. Chan, and O. Painter, "Coherent optical wavelength conversion via cavity optomechanics.," *Nat. Commun.*, vol. 3, p. 1196, Jan. 2012.

[64] S. Preble, L. Cao, A. Elshaari, A. Aboketaf, and D. Adams, "Single photon adiabatic wavelength conversion," *Appl. Phys. Lett.*, vol. 101, no. 17, p. 171110, 2012.

[65] J.-M. Mérolla, Y. Mazurenko, J.-P. Goedgebuer, and W. T. Rhodes, "Single-photon interference in sidebands of phase-modulated light for quantum cryptography," *Phys. Rev. Lett.*, vol. 82, pp. 1656–1659, Feb. 1999.

[66] P. S. Donvalkar, V. Venkataraman, S. Clemmen, K. Saha, and A. L. Gaeta, "Frequency translation via four-wave mixing Bragg scattering in Rb filled photonic bandgap fibers," *Opt. Lett.*, vol. 39, p. 1557, Mar. 2014.

[67] E. Zakka-Bajjani, F. Nguyen, M. Lee, L. R. Vale, R. W. Simmonds, and J. Aumentado, "Quantum superposition of a single microwave photon in two different "colour" states," *Nat. Phys.*, vol. 7, pp. 599–603, July 2011.

[68] I. Agha, S. Ates, L. Sapienza, and K. Srinivasan, "Spectral broadening and shaping of nanosecond pulses: toward shaping of single photons from quantum emitters.," *Opt. Lett.*, vol. 39, pp. 5677–80, Oct. 2014.

[69] J. Lavoie, J. M. Donohue, L. G. Wright, A. Fedrizzi, and K. J. Resch, "Spectral compression of single photons," *Nat. Photonics*, vol. 7, pp. 363–366, Mar. 2013.

[70] D. V. Reddy, M. G. Raymer, and C. J. McKinstrie, "Efficient sorting of quantum-optical wave packets by temporal-mode interferometry," *Opt. Lett.*, vol. 39, p. 2924, May 2014.

[71] A. S. Clark, S. Shahnia, M. J. Collins, C. Xiong, and B. J. Eggleton, "High-efficiency frequency conversion in the single-photon regime.," *Opt. Lett.*, vol. 38, pp. 947–9, Mar. 2013.

[72] K. Krupa, A. Tonello, V. V. Kozlov, V. Couderc, P. Di Bin, S. Wabnitz, A. Barthélémy, L. Labonté, and S. Tanzilli, "Bragg-scattering conversion at telecom wavelengths towards the photon counting regime.," *Opt. Express*, vol. 20, pp. 27220–5, Nov. 2012.

[73] H. J. McGuinness, M. G. Raymer, C. J. McKinstrie, and S. Radic, "Quantum frequency translation of single-photon states in a photonic crystal fiber," *Phys. Rev. Lett.*, vol. 105, no. 9, p. 93604, 2010.

[74] I. Agha, M. Davanço, B. Thurston, and K. Srinivasan, "Low-noise chip-based frequency conversion by four-wave-mixing Bragg scattering in SiN_x waveguides," *Opt. Lett.*, vol. 37, p. 2997, July 2012.

[75] R. H. Stolen, "Raman gain in glass optical waveguides," *Appl. Phys. Lett.*, vol. 22, p. 276, Oct. 1973.

[76] X. Li, J. Chen, P. Voss, J. Sharping, and P. Kumar, "All-fiber photon-pair source for quantum communications: Improved generation of correlated photons," *Opt. Express*, vol. 12, p. 3737, Aug. 2004.

[77] H. Takesue and K. Inoue, "1.5-um band quantum-correlated photon pair generation in dispersion-shifted fiber: suppression of noise photons by cooling fiber," *Opt. Express*, vol. 13, p. 7832, Oct. 2005.

[78] D. Méchin, R. Provo, J. D. Harvey, and C. J. McKinstrie, "180-nm wavelength conversion based on Bragg scattering in an optical fiber.," *Opt. Express*, vol. 14, no. 20, pp. 8995–8999, 2006.

[79] D. Kielpinski, J. Corney, and H. Wiseman, "Quantum optical waveform conversion," *Phys. Rev. Lett.*, vol. 106, p. 130501, Mar. 2011.

[80] M. Aspelmeyer, T. J. Kippenberg, and F. Marquardt, "Cavity optomechanics," *Rev. Mod. Phys.*, vol. 86, pp. 1391–1452, Dec. 2014.

[81] Z. Y. Ou and Y. J. Lu, "Cavity enhanced spontaneous parametric down-conversion for the prolongation of correlation time between conjugate photons," *Phys. Rev. Lett.*, vol. 83, pp. 2556–2559, Sept. 1999.

[82] C. E. Kuklewicz, F. N. C. Wong, and J. H. Shapiro, "Time-bin-modulated biphotons from cavity-enhanced down-conversion," *Phys. Rev. Lett.*, vol. 97, p. 223601, Nov. 2006.

[83] A. Kuzmich, W. P. Bowen, A. D. Boozer, A. Boca, C. W. Chou, L.-M. Duan, and H. J. Kimble, "Generation of nonclassical photon pairs for scalable quantum communication with atomic ensembles.," *Nature*, vol. 423, pp. 731–4, June 2003.

[84] C. H. van der Wal, M. D. Eisaman, A. André, R. L. Walsworth, D. F. Phillips, A. S. Zibrov, and M. D. Lukin, "Atomic memory for correlated photon states," *Science (80-.).*, vol. 301, pp. 196–200, July 2003.

[85] V. Balić, D. A. Braje, P. Kolchin, G. Y. Yin, and S. E. Harris, "Generation of Paired Photons with Controllable Waveforms," *Phys. Rev. Lett.*, vol. 94, p. 183601, May 2005.

[86] J. M. Donohue, M. Agnew, J. Lavoie, and K. J. Resch, "Coherent Ultrafast Measurement of Time-Bin Encoded Photons," *Phys. Rev. Lett.*, vol. 111, p. 153602, Oct. 2013.

[87] J. M. Donohue, J. Lavoie, and K. J. Resch, "Ultrafast Time-Division Demultiplexing of Polarization-Entangled Photons," *Phys. Rev. Lett.*, vol. 113, p. 163602, Oct. 2014.

[88] A. Christ, B. Brecht, W. Mauerer, and C. Silberhorn, "Theory of quantum frequency conversion and type-II parametric down-conversion in the high-gain regime," *New J. Phys.*, vol. 15, p. 053038, May 2013.

[89] J. M. Donohue, M. D. Mazurek, and K. J. Resch, "Theory of high-efficiency sum-frequency generation for single-photon waveform conversion," *Phys. Rev. A*, vol. 91, p. 033809, Mar. 2015.

[90] A. Eckstein, B. Brecht, and C. Silberhorn, "A quantum pulse gate based on spectrally engineered sum frequency generation.," *Opt. Express*, vol. 19, pp. 13770–8, July 2011.

[91] E. A. Dauler, M. E. Grein, A. J. Kerman, F. Marsili, S. Miki, S. W. Nam, M. D. Shaw, H. Terai, V. B. Verma, and T. Yamashita, "Review of superconducting nanowire single-photon detector system design options and demonstrated performance," *Opt. Eng.*, vol. 53, p. 081907, June 2014.

[92] M. Legre, R. Thew, H. Zbinden, and N. Gisin, "High resolution optical time domain reflectometer based on 1.55um up-conversion photon-counting module," *Opt. Express*, vol. 15, p. 8237, June 2007.

[93] P. Eraerds, M. Legre, J. Zhang, H. Zbinden, and N. Gisin, "Photon Counting OTDR: Advantages and Limitations," *J. Light. Technol.*, vol. 28, pp. 952–964, Mar. 2010.

[94] K. J. Blow, N. J. Doran, B. K. Nayar, and B. P. Nelson, "Two-wavelength operation of the nonlinear fiber loop mirror," *Opt. Lett.*, vol. 15, p. 248, Feb. 1990.

[95] E. Schrödinger and M. Born, "Discussion of probability relations between separated systems," *Math. Proc. Cambridge Philos. Soc.*, vol. 31, p. 555, Oct. 2008.

[96] A. Einstein, B. Podolsky, and N. Rosen, "Can Quantum-Mechanical Description of Physical Reality Be Considered Complete?," *Phys. Rev.*, vol. 47, pp. 777–780, May 1935.

[97] R. P. Feynman, "Simulating physics with computers," *Int. J. Theor. Phys.*, vol. 21, pp. 467–488, June 1982.

[98] D. Deutsch, "Quantum Theory, the Church-Turing Principle and the Universal Quantum Computer," *Proc. R. Soc. A Math. Phys. Eng. Sci.*, vol. 400, pp. 97–117, July 1985.

[99] M. A. Nielsen and I. L. Chuang, *Quantum computation and quantum information*. Cambridge: Cambridge University Press, 1st ed., 2004.

[100] J. L. O'Brien, "Optical quantum computing.," *Science*, vol. 318, pp. 1567–70, Dec. 2007.

[101] P. C. Humphreys, B. J. Metcalf, J. B. Spring, M. Moore, X.-M. Jin, M. Barbieri, W. S. Kolthammer, and I. A. Walmsley, "Linear Optical Quantum Computing in a Single Spatial Mode," *Phys. Rev. Lett.*, vol. 111, p. 150501, Oct. 2013.

[102] M. Malik, M. Mirhosseini, M. P. J. Lavery, J. Leach, M. J. Padgett, and R. W. Boyd, "Direct measurement of a 27-dimensional orbital-angular-momentum state vector.," *Nat. Commun.*, vol. 5, p. 3115, Jan. 2014.

[103] R. Fickler, R. Lapkiewicz, W. N. Plick, M. Krenn, C. Schaeff, S. Ramelow, and A. Zeilinger, "Quantum entanglement of high angular momenta.," *Science*, vol. 338, pp. 640–3, Nov. 2012.

[104] J. Roslund, R. M. de Araújo, S. Jiang, C. Fabre, and N. Treps, "Wavelength-multiplexed quantum networks with ultrafast frequency combs," *Nat. Photonics*, vol. 8, pp. 109–112, Dec. 2013.

[105] M. Brune, E. Hagley, J. Dreyer, X. Maître, A. Maali, C. Wunderlich, J. M. Raimond, and S. Haroche, "Observing the Progressive Decoherence of the 'Meter' in a Quantum Measurement," *Phys. Rev. Lett.*, vol. 77, pp. 4887–4890, Dec. 1996.

[106] C. G. Yale, B. B. Buckley, D. J. Christle, G. Burkard, F. J. Heremans, L. C. Bassett, and D. D. Awschalom, "All-optical control of a solid-state spin using coherent dark states.," *Proc. Natl. Acad. Sci. U. S. A.*, vol. 110, pp. 7595–600, May 2013.

[107] L. J. Rogers, K. D. Jahnke, M. H. Metsch, A. Sipahigil, J. M. Binder, T. Teraji, H. Sumiya, J. Isoya, M. D. Lukin, P. Hemmer, and F. Jelezko, "All-optical initialization, readout, and coherent preparation of single silicon-vacancy spins in diamond," *Phys. Rev. Lett.*, vol. 113, p. 263602, Dec. 2014.

[108] G. D. Fuchs, V. V. Dobrovitski, D. M. Toyli, F. J. Heremans, and D. D. Awschalom, "Gigahertz dynamics of a strongly driven single quantum spin.," *Science*, vol. 326, pp. 1520–2, Dec. 2009.

[109] C. Myatt, B. King, Q. Turchette, C. Sackett, D. Kielpinski, W. Itano, C. Monroe, and D. Wineland, "Decoherence of quantum superpositions through coupling to engineered reservoirs," *Nature*, vol. 403, pp. 269–73, Jan. 2000.

[110] M. Kasevich and S. Chu, "Atomic interferometry using stimulated Raman transitions," *Phys. Rev. Lett.*, vol. 67, pp. 181–184, July 1991.

[111] S. Ramelow, L. Ratschbacher, A. Fedrizzi, N. K. Langford, and A. Zeilinger, "Discrete Tunable Color Entanglement," *Phys. Rev. Lett.*, vol. 103, p. 253601, Dec. 2009.

[112] L. Olislager, J. Cussey, A. T. Nguyen, P. Emplit, S. Massar, J.-M. Merolla, and K. P. Huy, "Frequency-bin entangled photons," *Phys. Rev. A*, vol. 82, p. 013804, July 2010.

[113] K. Krupa, M. Bettenzana, A. Tonello, V. Couderc, P. Di Bin, S. Wabnitz, and A. Barthélémy, "Bragg-scattering four-wave mixing in nonlinear fibers with intracavity frequency-shifted laser pumps," *Int. J. Opt.*, vol. 2012, pp. 1–7, 2012.

[114] R. V. Roussev, C. Langrock, J. R. Kurz, and M. M. Fejer, "Periodically poled lithium niobate waveguide sum-frequency generator for efficient single-photon detection at communication wavelengths," *Opt. Lett.*, vol. 29, p. 1518, July 2004.

[115] A. L. Jones, "Coupling of Optical Fibers and Scattering in Fibers," *J. Opt. Soc. Am.*, vol. 55, p. 261, Mar. 1965.

[116] B. M. Rodríguez-Lara, F. Soto-Eguibar, and D. N. Christodoulides, "Quantum optics as a tool for photonic lattice design," *Phys. Scr.*, vol. 90, p. 068014, June 2015.

[117] J. Mower, Z. Zhang, P. Desjardins, C. Lee, J. H. Shapiro, and D. Englund, "High-dimensional quantum key distribution using dispersive optics," *Phys. Rev. A*, vol. 87, p. 062322, June 2013.

[118] I. Ali-Khan, C. J. Broadbent, and J. C. Howell, "Large-Alphabet Quantum Key Distribution Using Energy-Time Entangled Bipartite States," *Phys. Rev. Lett.*, vol. 98, p. 060503, Feb. 2007.

[119] S. P. Walborn, D. S. Lemelle, M. P. Almeida, and P. H. S. Ribeiro, "Quantum key distribution with higher-order alphabets using spatially encoded qudits," *Phys. Rev. Lett.*, vol. 96, p. 090501, Mar. 2006.

[120] B. Brecht, A. Eckstein, R. Ricken, V. Quiring, H. Suche, L. Sansoni, and C. Silberhorn, "Demonstration of coherent time-frequency Schmidt mode selection using dispersion-engineered frequency conversion," *Phys. Rev. A*, vol. 90, p. 030302, Sept. 2014.

[121] A. L. Migdall, D. Branning, and S. Castelletto, "Tailoring single-photon and multiphoton probabilities of a single-photon on-demand source," *Phys. Rev. A*, vol. 66, p. 053805, Nov. 2002.

[122] J. H. Shapiro and F. N. Wong, "On-demand single-photon generation using a modular array of parametric downconverters with electro-optic polarization controls," *Opt. Lett.*, vol. 32, p. 2698, Sept. 2007.

[123] E. Jeffrey, N. A. Peters, and P. G. Kwiat, "Towards a periodic deterministic source of arbitrary single-photon states," *New J. Phys.*, vol. 6, pp. 100–100, July 2004.

[124] T. B. Pittman, B. C. Jacobs, and J. D. Franson, "Single photons on pseu-

dodemand from stored parametric down-conversion," *Phys. Rev. A*, vol. 66, p. 042303, Oct. 2002.

[125] M. J. Collins, C. Xiong, I. H. Rey, T. D. Vo, J. He, S. Shahnia, C. Reardon, T. F. Krauss, M. J. Steel, A. S. Clark, and B. J. Eggleton, "Integrated spatial multiplexing of heralded single-photon sources.," *Nat. Commun.*, vol. 4, p. 2582, Jan. 2013.

[126] J. Mower, N. C. Harris, G. R. Steinbrecher, Y. Lahini, and D. Englund, "Towards high-fidelity quantum computation and simulation on a programmable photonic integrated circuit," June 2014.

[127] A. Peruzzo, M. Lobino, J. C. F. Matthews, N. Matsuda, A. Politi, K. Poulios, X.-Q. Zhou, Y. Lahini, N. Ismail, K. Wörhoff, Y. Bromberg, Y. Silberberg, M. G. Thompson, and J. L. OBrien, "Quantum walks of correlated photons.," *Science*, vol. 329, pp. 1500–3, Sept. 2010.

[128] E. Farhi and S. Gutmann, "Quantum computation and decision trees," *Phys. Rev. A*, vol. 58, pp. 915–928, Aug. 1998.

[129] S. Aaronson and A. Arkhipov, "The Computational Complexity of Linear Optics," *Theory Comput.*, vol. 9, no. 4, pp. 143–252, 2013.